科技部補助專題研究計畫成果報告
期末報告

具有可見光與近紅外光吸收能力的光敏感兩親性樹枝狀分子載體:材料合成與光誘導控制釋放性質分析

計 畫 類 別 ： 個別型計畫
計 畫 編 號 ： MOST 104-2119-M-040-001-
執 行 期 間 ： 104年08月01日至105年12月31日
執 行 單 位 ： 中山醫學大學醫學應用化學系(含碩士班)

計 畫 主 持 人： 朱智謙

計畫參與人員： 碩士級-專任助理人員：游蕙綺
碩士班研究生-兼任助理人員：廖名嘵
碩士班研究生-兼任助理人員：王珈宜
大專生-兼任助理人員：江家儀
大專生-兼任助理人員：陳皓宇
大專生-兼任助理人員：林姿妘

中 華 民 國 106 年 03 月 26 日

中 文 摘 要 ： 近年來，透過跨領域結合材料設計合成與生物醫學臨床應用，開發具有腫瘤標靶功能且能精準控制釋放的藥物或基因載體系統為一個熱門的研究方向。本年度研究計畫主要是利用光來驅動控制釋放(如光二極體、雷射等)，在指定的時間與位置將生物活性分子快速釋放出來，以達成精準控制的目的。另外，為了增加光源對於生物組織的穿透深度，我們也開發了近紅外光驅動的光敏感系統，以達到深層治療的效果。研究成果之一為利用可進行光誘導裂解的香豆素衍生物作為核心，連結膽固醇與樹枝狀分子形成兩親性結構。此載體可於水中或氣液界面自我組裝成樹枝狀高分子微胞或Langmuir單分子薄膜，並對於DNA分子有極佳的結合力。利用光二極體的照射可以簡單驅動光裂解反應，並將DNA釋放出來以達到基因轉染的目的。成果二則是製備出結合能量上轉換晶體、樹枝狀高分子、光敏劑的奈米複合材料，並以近紅外光雷射來驅動光動力療法。我們也發現此系統對於癌球細胞具有深層治療的效果，而癌球細胞核心通常具有顯著的癌幹細胞特質，與癌症復發與轉移高度相關，因此我們的系統在臨床治療上極具潛力，目前已進入活體實驗的階段。

中 文 關 鍵 詞 ： 香豆素、光敏感、藥物傳遞系統、能量上轉換、基因載體、光動力療法

英 文 摘 要 ： Recently, developing smart drug or gene delivery systems with tumor-targeting and precise control/release properties has aroused much interests in the interdisciplinary fields of chemical synthesis and biomedicine. In this project, we focus on the development of photo-triggered delivery systems that can release bioactive molecules under a spatiotemporal control of light stimulation. Moreover, to enhance tissue penetration depth, we also developed a hybrid nanoparticle system responsive to near-infrared light for achieving efficient clinical therapy. The first report summaries a photoresponsive amphiphilic dendrons that can assemble into a pseudodendrimer in aqueous solution and into a Langmuir monolayer at air/water interface. The self-assembled structures exhibit strong binding with plasmid DNA, and thus-formed dendriplexes can be readily dissociated under light exposure. Accordingly, the DNA can be photo-released to perform gene transfection. The second report summaries a hybrid nanoparticle combining an upconversion nanocrystal, dendrimers, and photosensitizers. This nanosystem is capable of performing near-infrared light-triggered photodynamic therapy toward tumorspheres with a cancer stem cell property, and in vivo study is now underway.

英 文 關 鍵 詞 ： Coumarin, photoresponsive, drug delivery system, energy upconversion, gene vector, photodynamic therapy

成果報告簡介

隨著蛋白質體學（proteomics）的發展，人類在對抗重大疾病上採取了新的思維與策略，希望針對已知會造成疾病的關鍵蛋白質，找出合適的藥物來控制它；然而基因療法走的卻是另外一條路徑，希望藉由控制基因表現讓細胞主動停止製造這些致病蛋白。而站在奈米科技的角度，前者就像是由上往下（top-down）的治療方式，而後者就是由下往上（bottom-up）的途徑希望達到一樣的效果。尤其是反義(antisense)策略之基因療法受到極大的矚目，希望能夠藉由控制基因來破壞messenger RNA的轉譯作用，進而抑制關鍵蛋白質的生成。一般而言，核酸分子在生物體環境中並不穩定，且結構帶有負電無法有效的進入細胞中進行轉染作用。所以目前有兩種方法來克服這些使用上的難題，其一是藉由化學合成法來修飾核酸分子原本的結構，讓其更能夠抵抗生理環境所造成的破壞，但是結構經過修飾後的核酸分子卻有可能失去原本的基因轉染功能。另外一個方法就是利用有效率的載體將不穩定的核酸分子帶進細胞內進行轉染工作，控制基因的表現與蛋白質的生成。

近年來，我們實驗室一直在探討利用兩親性樹枝狀分子衍生物作為基因載體的能力，而先前的研究結果發現水溶性碳六十衍生物就算在很低的濃度之下，都會產生類似微胞(micelle)結構的奈米聚集體。我們進一步利用攜帶正電荷的碳六十衍生物所形成的奈米粒子作為DNA載體，並發現兩者之間結合能力強，在很低的N/P ratio下就可以形成穩定的複合體，且粒徑約為150 nm。而MCF-7與HeLa兩種細胞對於此複合體的吞噬效率很高，可與一般市售的陽離子型高分子載體相比，但是進入細胞後，整體基因轉染的效率卻只有高分子載體的一半。我們推測碳六十衍生物雖然能夠與DNA有效的結合，卻有可能因為結合力太強，而降低DNA從核內體endosome釋放出來的效率，讓基因轉染無法達到預期的效果。為了克服這個問題，我們在兩親性結構中引入光敏感基團，合成了一系列具有光敏感特性的兩親性樹枝狀分子載體，親疏水兩端分別為PAMAM與膽固醇分子。在水中可以自組裝形成微胞並且有效包覆DNA分子。而在in vitro實驗中，照射UV光使得光敏感基團會快速裂解，破壞微胞結構後讓DNA可以被釋放出來。

在本年度計畫中，我們持續開發光敏感載體，主要是利用香豆素衍生物為核心，並透過光誘導的方式將生物活性分子釋放出來，以達到時間與空間控制釋放的效果。同時為了降低紫外光對於生物組織的傷害，我們也透過分子設計來延長香豆素衍生物的共軛長度，以提高對於藍光波段的吸收能力。另外，我們也依循兩個策略來完成利用近紅外NIR光驅動臨床癌症治療的目的，其一為合成具有雙光子吸收效率的香豆素衍生物，利用高能量脈衝雷射光來達成藥物釋放的目的；其二為利用能量上轉換奈米晶體UCNP做為載體核心，合成出具有執行光動力療法能力的奈米複合材料。

成果報告1主要為利用香豆素衍生物作為核心合成出兩性樹枝狀分子載體C-IG1。C-IG1在水中可自我組裝成psuedodendrimer，且其臨界聚集濃度約為40 μM，遠低於一般的兩性界面活性劑分子。我們也利用Langmuir單層薄膜法搭配螢光顯微鏡來分析C-IG1在air-water界面的自我組裝能力。而不管在水中或是氣液界面，上述奈米聚集結構都可以在照光後產生光裂解反應，預期可以順利透過光控釋放生物活性分子。另外利用香豆素分子本質性螢光，可以直接分析載體對於生物活性分子的結合能力與釋放能力。成果報告2則是開發對於NIR光敏感的奈米複合材料，我們利用能量上轉換晶體作為核心來驅動光動力療法，並將樹枝狀高分子吸附在奈米粒子的表面，除了能夠提高水溶性，並可以增加被細胞吞噬的能力。最後透過靜電作用力吸附光敏劑分子來執行光動力療法。我們發現利用NIR光可以對於具有三維構造的癌球細胞，產生深層治療的效果，而癌球細胞的內部核心通常具有明顯的癌幹細胞的特質，因此我們所開發出來的材料具有運用在臨床治療上的潛力，目前in vivo實驗也在進行中。

成果報告 1

Title: Amphiphilic dendron containing a photocaged coumarin derivative as a DNA carrier:

1. INTRODUCTION

Phototriggers provide a useful strategy for the photocontrolled drug delivery system (DDS) because they enable rapid and accurate spatial and temporal control with external light stimulation. The biological relevant materials containing photocaged building blocks can undergo efficient photolysis through active phototriggers, thereby leading to structural degradation combined with the release of bioactive payloads. One of the most well-known light-absorbing photocages is the coumarin family, which enables one- or two-photon–regulated drug release.[1-5] Because coumarin derivatives undergo photosolvolysis through a photo S_N1 mechanism, the microenvironment for achieving effective bond cleavage requires access to a nucleophile in a protic media (typically water).[6] Furthermore, the intrinsic fluorescent nature of the coumarin ring makes these photocages robust fluorescent probes for simultaneously imaging the biodistribution of the DDS in living tissues.[3]

The use of amphiphilic dendron architectures, in which hydrophobic groups at the focal point form pseudodendrimers through a self-assembly process, has facilitated a new type of dendrimer-mediated delivery *in vitro* and *in vivo*. Notably, this supramolecular strategy, which enables combining the characteristics of polymers and lipids, can give lead to a synergistic effect, particularly during nucleic acid delivery. Several research groups have demonstrated remarkable gene transfection mediated by these amphiphilic dendrons. Principally, when used as gene vectors, pseudodendrimers apply dynamic and responsive association and dissociation toward nucleic acids. Moreover, complete dendron degradation may be required for effective decomplexation to release nucleic acids. However, experimental and computer-aided simulation data have revealed that the structural degradation of dendrons when bound to nucleic acids becomes ineffective on the transfection timescale, even at lower pH associated with endosomes. This key problem makes gene delivery a challenging task, particularly for the *in vivo* system.

In this study, we developed amphiphilic dendritic scaffolds with photocages for creating a photoresponsive pseudodendrimer that can achieve controlled release under an active light trigger. The amphiphilic structure composed of a hydrophilic poly(amido amine) (PAMAM) dendron and lipophilic cholesterol molecule combines the advantageous gene delivery features of both lipids and polymer vectors. As shown in Figure 1, the amphiphilic counterpart is further interconnected by a photolabile coumarin ester, enabling the photoinduced degradation of the amphiphilic structure. The arrow indicates an electrophilic allylic carbon, and the C-O bond can be readily cleaved in the presence of nucleophiles under light illumination. Consequently, this strategy provides an active route for accelerating nucleic acid release and enhancing gene transfection efficiency. Moreover, to understand the self-assembly process of the amphiphiles and their photoresponsive behavior, the Langmuir technique was introduced for investigating the interfacial phenomenon at the air–water interface. We believe that the thus-formed Langmuir monolayers are more fluid and therefore provide a more realistic model for studying DNA binding and phototriggered release.

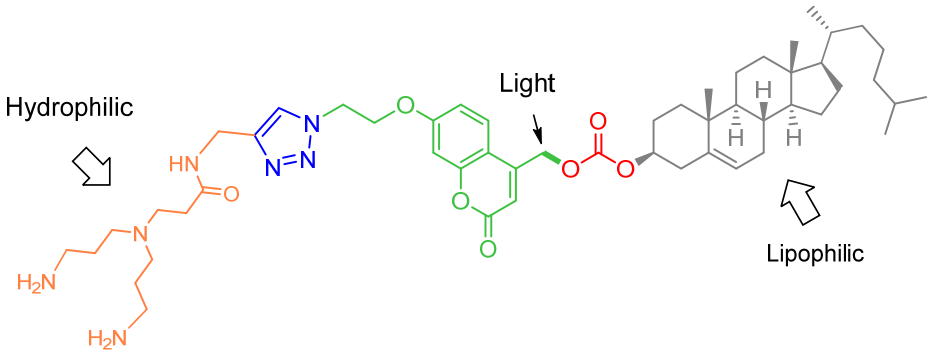

Figure 1. Chemical structure of C-IG_1.

2. RESULTS AND DISCUSSION

As shown in Scheme 1, the azide-functionalized cholesterol and coumarin conjugate ***1*** were synthesized from a commercially available 7-hydroxy-4-methylcoumarin in four steps. On the basis of our design, the cholesterol not only acts as the lipophilic head but also assists cellular uptake by enhancing penetration across a cell membrane. The interconnecting coumarin-derived carbonate ester is highly sensitive to ultraviolet (UV) light, and the photolabile C-O bond (marked in bold) is readily cleaved to recover compound ***2*** and release a free cholesterol molecule. Copper(I)-catalyzed azide-alkyne cycloaddition (CuAAC) between the alkyl-functionalized PAMAM dendrons and ***1*** affords the amphiphilic dendrons, namely C-IG_1 (Figure 1). Notably, compared with the conventional PAMAM dendron, this dendritic analogue has two additional primary amine terminals but possesses an inverse tertiary amine branch and amide linkage. Here, the amphiphilic dendron was well-characterized through nuclear magnetic resonance (NMR) and mass spectrometry (MS) analysis (see Supporting Information). The click conjugation was confirmed according to the appearance of triazole proton resonance, and the observed mass values were consistent with the calculated values of the protonated adducts of C-IG_1.

The time-dependent photolytic reaction of ***1*** was monitored by UV–Vis absorption and fluorescence spectra. The maximum absorption and emission wavelengths of ***1*** were found to be 320 and 390 nm, respectively. As shown in Figure 2a, the absorbance at 320 nm decreases slightly as the sample solution is exposed to a 365-nm light emitting diode (LED); however, the fluorescence intensity at 390 nm gradually increases with the irradiation time (Figure 2b). The fluorescence enhancement is evidently attributable to the S_N1-like photolytic reaction of the coumarin ester with an increasing fluorescence quantum yield. Moreover, high-performance liquid chromatography (HPLC) analysis showed the depletion of the retention peak of ***1*** after light exposure (Figure 2c). Gas chromatography (GC)–MS analysis further confirmed the released cholesterol through photocleavage as the characteristic elution peak (Figure 2d). All results suggested a successful photoinduced structural degradation of the coumarin derivative.

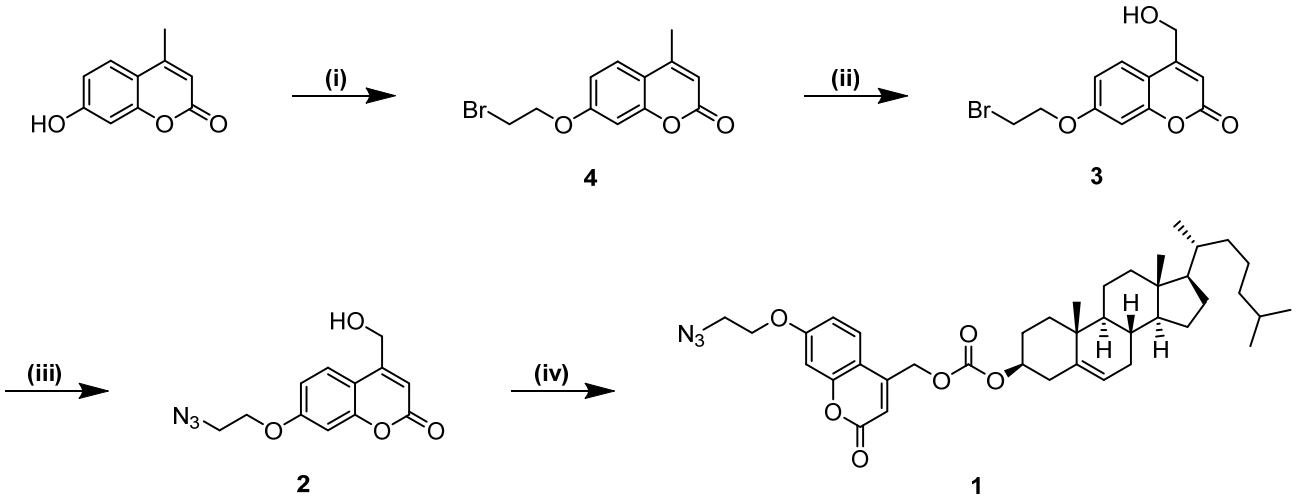

Scheme 1. Synthetic route.

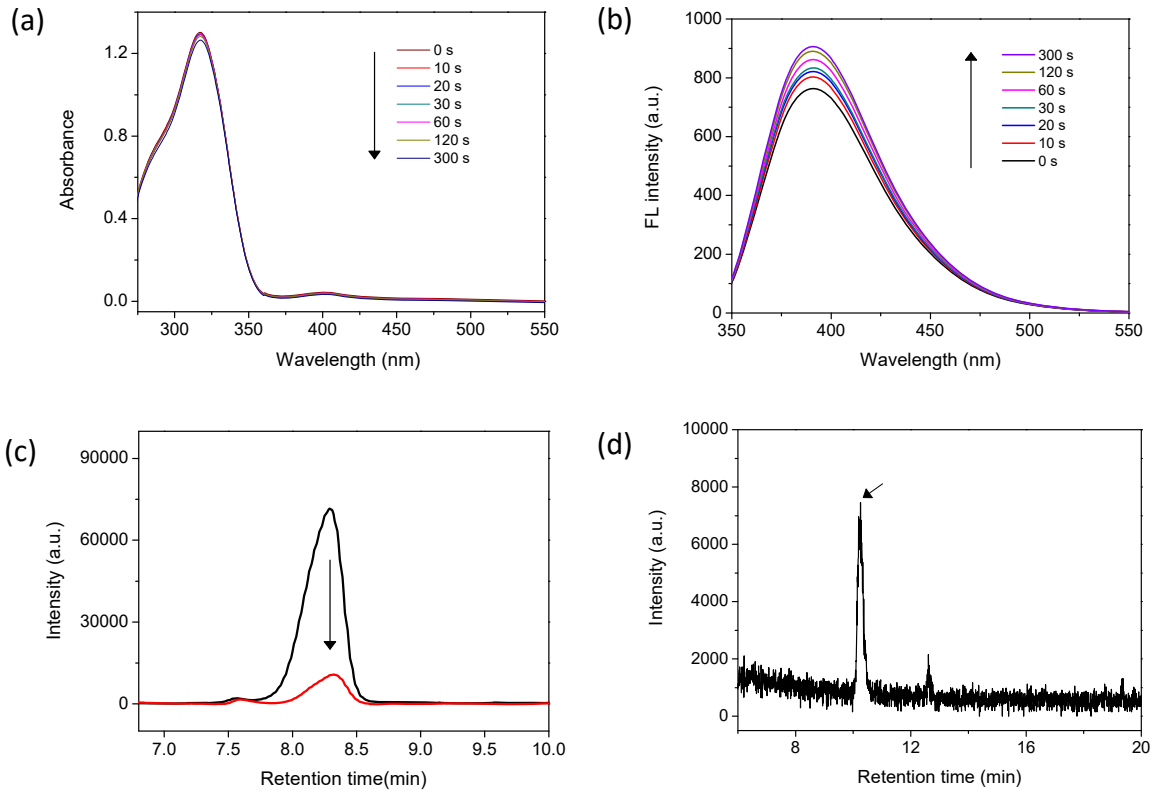

Figure 2. The analysis for photoresponsive behavior.

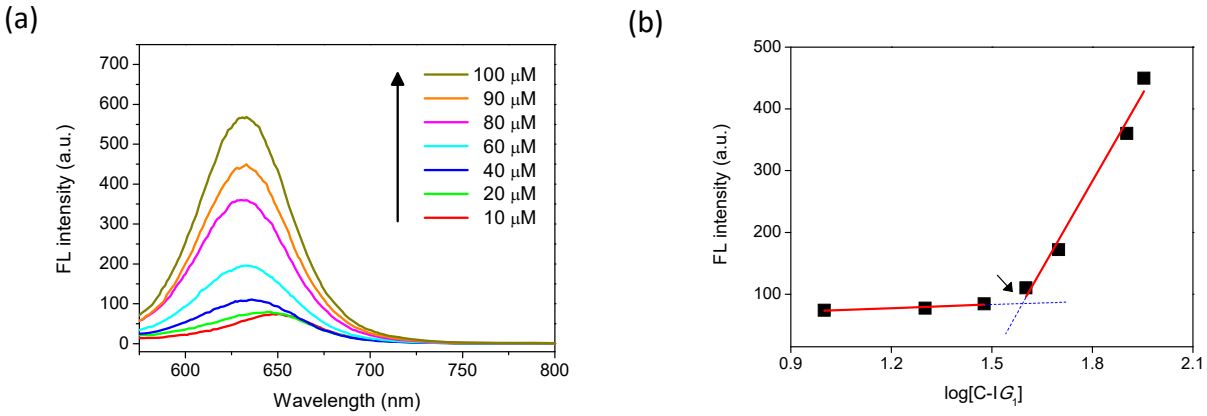

Figure 3. The analysis for the formation of pseudodendrimers.

Because of the amphiphilic structure being composed of a hydrophilic PAMAM dendron and a lipophilic cholesterol, C-IG_1 could self-assemble into Percec-type pseudodendrimers with micelle-like structures in an aqueous medium. This self-assembly process was confirmed using a Nile red solubilization fluorescence assay to detect the formation of a hydrophobic domain of cholesterol within an assembled nanostructure. In this assay, the hydrophobic stain Nile red was gradually solubilized in the micelles and emit red fluorescence as the concentration of C-IG_1 increases (Figure 3a). Figure 3b shows self-assembly with discontinuity in the fluorescence intensity of Nile red at 635 nm, plotted against the increasing dendron concentration at the critical aggregation concentration (CAC). The CAC for C-IG_1 was approximately 39 μM, much lower than that for a coumarin-derived surfactant. This result suggests the amphiphilic dendrons possess more effective self-assembly process.

To understand the self-assembly behavior of the amphiphile, the Langmuir technique was introduced to investigate the interfacial phenomenon at the air–water interface. As shown in Figure 4a, π-A isotherms have three distinguishable phase transitions from a gas (i)-like state to liquid (ii)- and finally solid (iii)-like states, suggesting that C-IG_1 possesses significant compressibility, eventually forming homogeneous Langmuir monolayers upon compression, until the surface pressure of collapse is approximately 50 mN/m. This result evidently suggests that the amphiphilic structure also favors the molecular assembly at the air–water interface. The final molecular area (A_0) in a compressed film determined by extrapolation to zero surface pressure is approximately 36 Å^2 for C-IG_1, consistent with the A_0 of the amphiphilic dendrons with small dendritic branches. Moreover, the interfacial morphology of the Langmuir film under increasing surface pressures was analyzed by incorporating Nile red probes with in situ monitoring through fluorescence microscopy. Figure 4b–d denotes the fluorescence distributions of the probe molecules under different molecular packings of the amphiphiles in the three states. Figure 4d illustrates the closely packed and highly fluorescent spots under the surface pressure of 50 mN/m, suggesting the successful formation of a condensed Langmuir monolayer at the interface. This result corroborates with that of the solubilization assay analysis that the emission intensity considerably increases in the presence of the micelle-like assembled structure of the amphiphiles in water. This result also confirms that the C-IG_1 possesses a strong self-assembly capability in both aqueous phases and at the air–water interface.

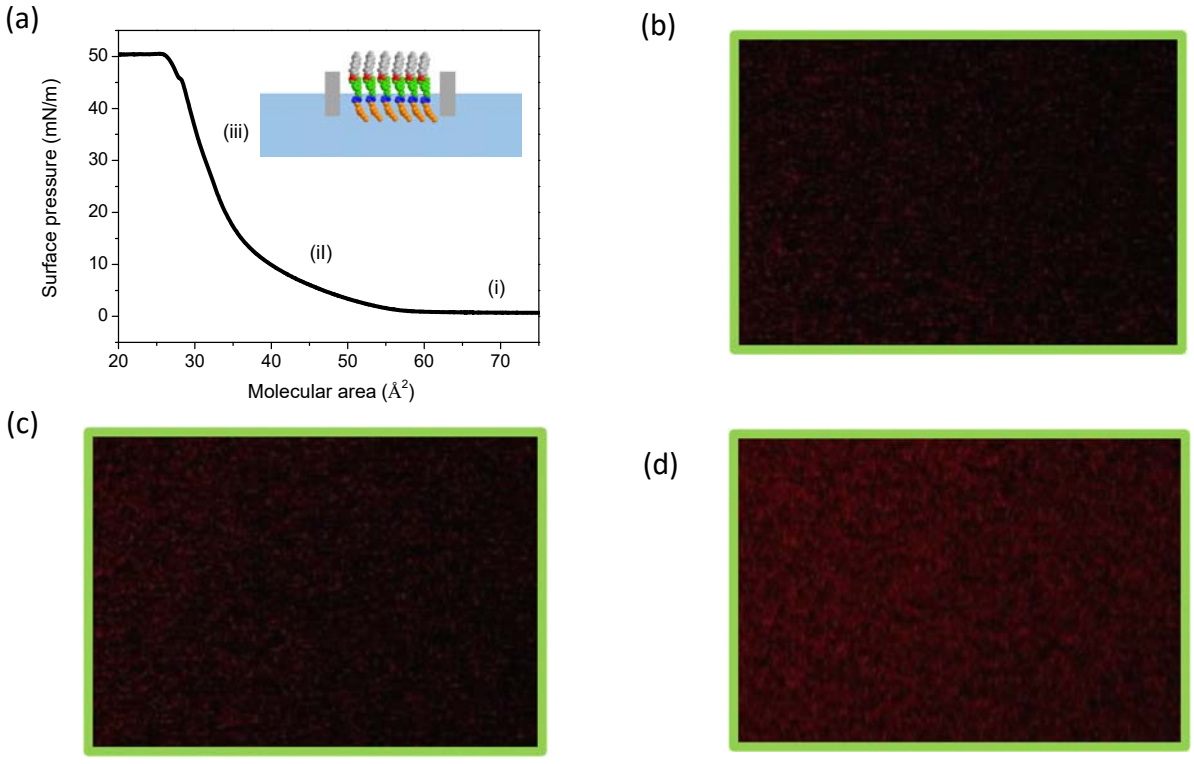

Figure 4. Langmuir analysis.

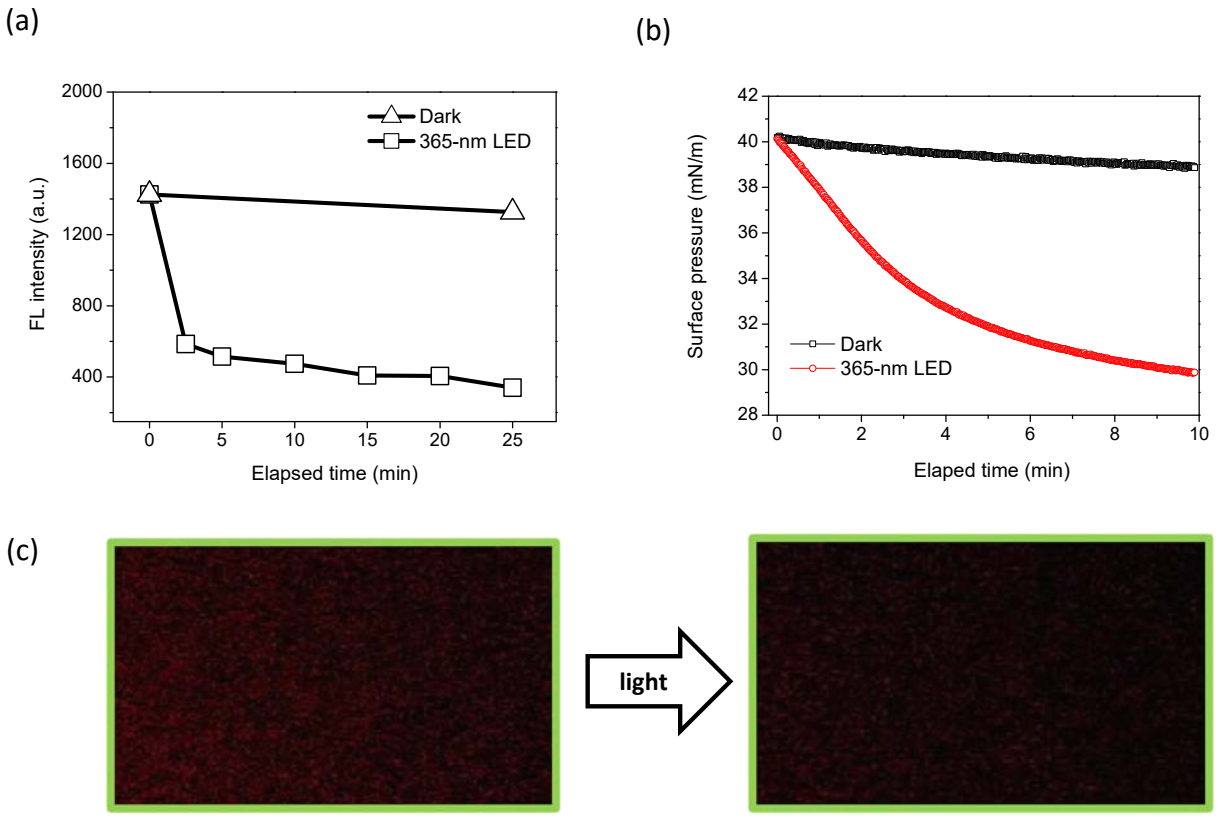

Figure 5. The photoresponsive behavior at air-water interface.

After confirming that the amphiphilic dendron can process molecular assembly, we examined the photoresponsive behavior of the assembled structures. The photocleavable building block of coumarin ester aids the self-aggregated micelles in readily dissociating under UV irradiation. First, this deformation can be analyzed using micelle-encapsulated Nile red probes. In contrast to the controlled experiment, where the solution stored in darkness only exhibited a slight decrease in fluorescence intensity, 365-nm light irradiation can cause a considerable fluorescence decrement within 5 min, until reaching a plateau (Figure 5a). This result suggests that the micelles are stable until active light stimulation degrades these self-assembled structures. Second, a Langmuir monolayer at a certain surface pressure (approximately 40 mN/m) and molecular area, maintained by keeping the barriers constant, was prepared. Subsequently, the equilibrium was continuously disturbed through 365-nm light irradiation. Before analysis, control experiment showed that the surface pressure of the monolayer of stearic acids remains constant on light irradiation, suggesting that if the amphiphile is insensitive to UV light, light stimulation does not influence the integrity of the assembled structure. Figure 5b shows the correlation of elapsed time (t) versus surface pressure, recorded immediately after photostimulation was activated (t = 0). The surface pressure of the monolayer composed of C-IG_1 gradually decreases as the light is turned on (red line); by contrast, this monolayer remains relatively stable in darkness (black line). Notably, the nonlinear decay of the surface pressure following light excitation may be attributable to the first-order kinetics of the S_N1-like photolysis mechanism for coumarin derivatives, because the reaction rate is correlated only with the initial C-IG_1 concentration and the photoinduced dissociation of C-IG_1 to yield a carbocation intermediate is the rate-determining step for the overall photolytic reaction. In addition, in situ monitoring of the interface morphology by using Nile red probes also indicated that the fluorescence intensity for the assembled pattern decreased on light excitation (Figure 5c). The visualized images clearly confirm the efficient photodegradation of the Langmuir monolayer.

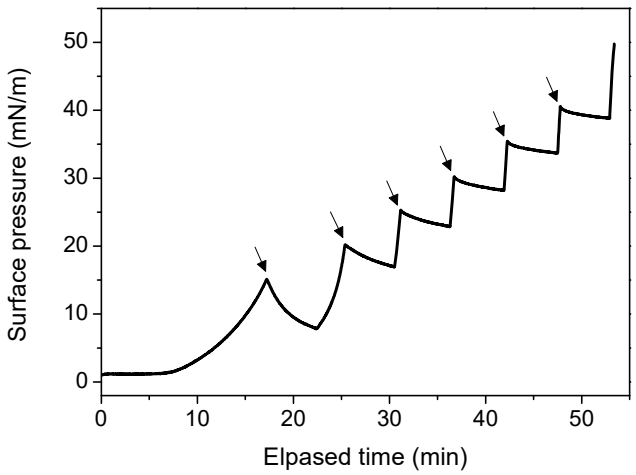

Figure 6. The photoresponsive behavior at air-water interface.

As shown in Figure 6, the monolayer at the interface partially collapsed on light exposure because it could be reconstructed through continuous compression in darkness. The surface pressure initially decreased upon light excitation (black arrows) but increased again after barrier compression in darkness. The photoinduced collapse and reconstruction of the monolayer can be alternatively manipulated until the maximum pressure of approximately 50 mN/m is reached. Taken together, in the Langmuir technique, the assembled structure composed of coumarin-based amphiphilic dendrons is consistently highly sensitive to UV light. The bond cleavage between the coumarin ester and cholesterol at the interface results in the collapse of the monolayer under light stimulation. The current Langmuir analysis also confirmed that the photostimulation strategy provides accurate spatial and temporal control over the self-assembled system integrity.

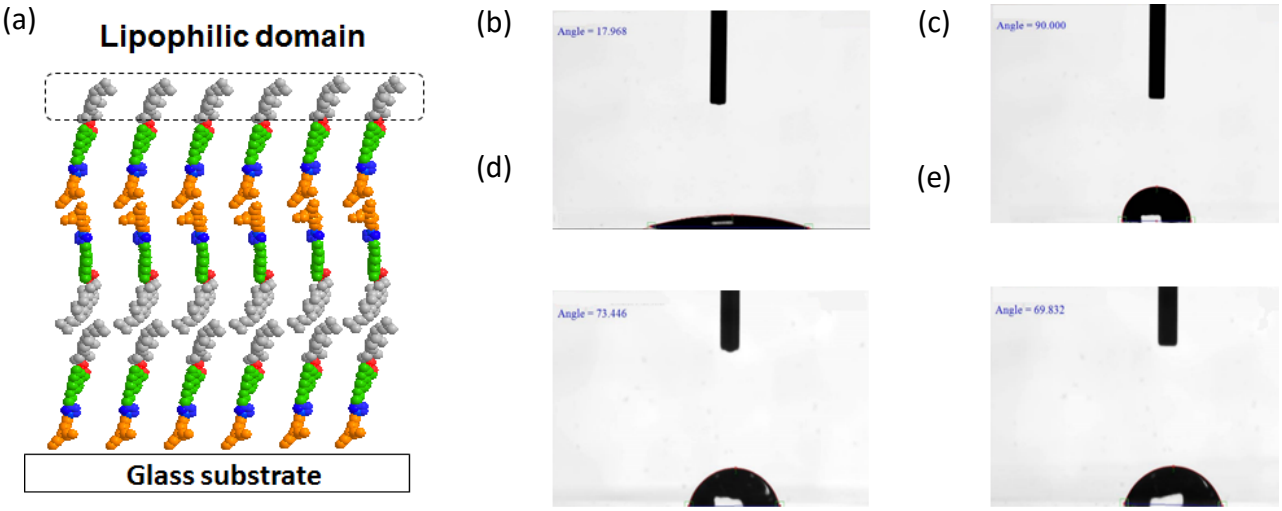

Figure 7. Contact angle analysis.

To further reveal the thin-film properties of the amphiphilic C-IG_1, three-layer monolayers were transferred to a glass substrate by using up–down–up strokes based on the Langmuir–Blodgett (LB) technique. Because the coverglass possesses a hydrophilic surface, the bottom layer of the sandwich structure comprises the hydrophilic PAMAM dendron and the upper layer should comprise lipophilic cholesterols (Figure 7a). From the measurement of static contact angles (Figure 7b–e), the angle for a water drop on the surface considerably increases from approximately 18° to 90° after three-layer

film deposition. This result confirms that the surface becomes a lipophilic domain because of a tidy arrangement of the amphiphiles. Notably, the contact angles gradually decrease when the film is exposed to UV light, implying that the ordering LB film is disturbed by an incident light. The photolabile coumarins undergoing a photolytic reaction cause the structural degradation of the amphiphiles. Accordingly, the LB film of C-IG_1 also exhibits a photoresponsive behavior in a solid state.

After the coumarin-based amphiphilic dendrons self-aggregate into the assembled pseudodendrimers with positively charged peripherals, they can effectively interact with polyanionic bioactive targets, such as DNA, to form dendriplexes through electrostatic interaction. The binding ability of C-IG_1 toward cyclic DNA, a pEGFP-C1 reporter gene (approximately 4700 bp), was first studied through fluorescence titration experiments. In Stern–Volmer analysis, the intrinsic fluorescence of the coumarin moiety enables direct resolution of the binding affinity of the vector and DNA. As shown in Figure 8, the emission intensity of coumarin at $\lambda = 390$ nm gradually decreased with the continuous addition of DNA as the fluorescence quencher, indicating successful binding between the pseudodendrimers and giant DNA through electrostatic association. The Stern–Volmer plot (inset in Figure 8) further illustrates a linear correlation between the change in fluorescence intensity and concentration of the quencher, suggesting a static quenching mode for both species. Assuming that the molecular mass for cyclic DNA is approximately 3×10^6 Da, the quenching constant retrieved from the slope is 0.998 μg^{-1}, corresponding to 5.9×10^9 M^{-1}. The value is close to the magnitude of the binding affinity between polymers and proteins rather than that of the groove binding of small molecules (e.g., drug) and DNA. Thus, the pseudodendrimer assembled from amphiphilic C-IG_1 is an excellent biomacromolecular binder and the dendriplex formation is a ground-state macromolecular complexation process occurring through polyvalent interactions.

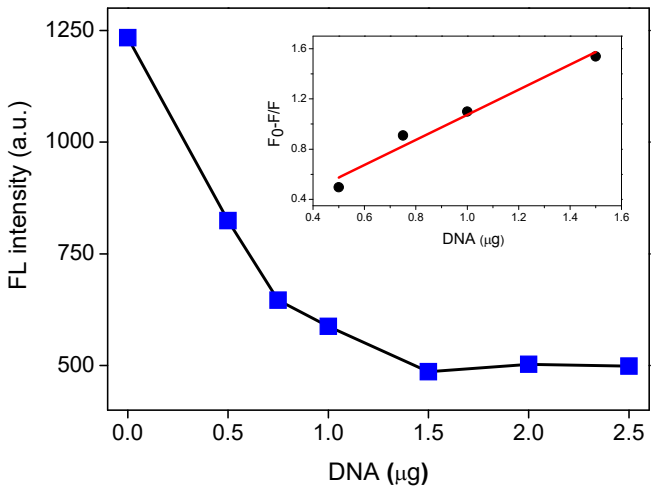

Figure 8. Fluorescence titration and Stern-Volmer analysis.

The binding and photoinduced release were analyzed using an ethidium bromide (EtBr) displacement assay. This assay method involves using the competition between the DNA binder and EtBr to determine the concentration at which the DNA binder takes effect. This concentration can be expressed as charge excess (CE_{50}) which reflects the concentration of the DNA binder required for half of the EtBr to be displaced from binding to DNA. This value is also the equivalent of a minimum nitrogen-to-phosphorus (N/P) ratio that is typically used to determine the amount of amine-based binding motifs required for effective DNA condensation through electrostatic interactions between amine and phosphate groups.

Figure 9a shows the fluorescence titration experiment by increasing C-IG_1 concentration at constant amounts of DNA (0.5 μg) and EtBr (0.7 μg). Initially, the EtBr undergoes a large increase in fluorescence intensity on intercalation with stacks of nucleic acid base pairs. However, the fluorescence quenching of the EtBr/DNA complexes occurs in the presence of amine-based vectors,

engendered by the competitive displacement of EtBr by the vectors. The emission intensity at 590 nm gradually decreases as the N/P ratio increases, suggesting increasing dendriplex formation with increasing C-IG_1 concentration. Here, CE_{50} calculated from the titration data was less than 1, consistent with the results of a previous study using cholesteryl-derived amphiphilic PAMAM dendrons as DNA vectors. Moreover, when the vectors degrade under UV light exposure, DNA should be released and EtBr should reintercalate into the double helix, thus reactivating its fluorescence. Accordingly, Figure 9b shows the fluorescence increment from the minimum intensity of the DNA/C-IG_1 complexes at N/P ratio = 2 after LED light excitation. By contrast, the fluorescence intensity remained static when the complex solution was maintained in darkness. This result confirms that the photolytic reaction of the vectors induces decomplexation accompanied by DNA release through an active phototriggered route.

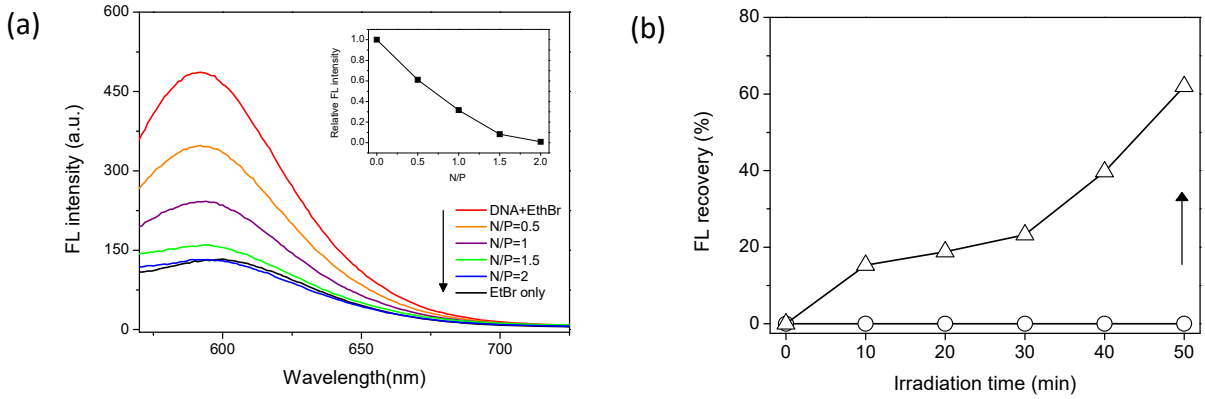

Figure 9. DNA binding and releasing.

After light exposure for 50 min, the fluorescence intensity was partially recovered to approximately 60% of the original magnitude for the emission of the DNA/EtBr complex in the absence of the dendritic vectors (N/P = 0). This result implies that only 60% of DNA is released from the dendriplexes upon light excitation. Thus, the assembled dendrons may be more resistant to the photoinduced disruption than a single dendron is. The Langmuir analysis results also revealed that the assembled structure would soon be recovered under external compression after a partial collapse. Therefore, these electrostatic complexes may be relatively resistant to environmental fluctuation. Although UV light is insufficient to induce complete dissociation of the DNA complexes using a coumarin-derived amphiphilic dendron as the vector, it does assist nucleic acid release.

3. CONCLUSIONS

In summary, we successfully synthesized photoresponsive amphiphilic PAMAM dendrons bearing photolabile coumarin ester building blocks as DNA carriers. The amphiphilic dendrons C-IG_1 exhibit the capability for self-assembly during micelle-like pseudodendrimer formation in an aqueous solution, which was confirmed by spectroscopy and Langmuir isotherm analysis. Based on the bipolar functionality, C-IG_1 also demonstrates substantial binding affinity with cyclic DNA at low N/P ratios. Notably, the thus-formed DNA complexes readily dissociate under UV light irradiation because the coumarin ester group in the dendritic structure undergoes efficient photolytic cleavage, causing effective dendron degradation accompanied by DNA release.

4. EXPERIMENTAL SECTIONS

4.1 Materials and Instruments. The chemical reagents and organic solvents for materials synthesis were obtained as high-purity reagent-grade from commercial suppliers and used without further purification. Synthesis of compound **1-4** and *tert*-butyloxycarbonyl (Boc)-protected IG_1 was described in supporting information. ^{1}H (400 MHz) and ^{13}C (75 MHz) NMR spectra were recorded on a Varian Mercury Plus 400 MHz spectrometer at room temperature using $CDCl_3$, DMSO-d_6, methanol-d_4, or D_2O as the solvents. Spectral processing (Fourier transform, peak assignment, and integration) was

performed using MestReNova 6.2.1 software. Matrix-assisted laser desorption ionization/time-of-flight (MALDI–TOF) MS was performed on a Bruker AutoFlex III TOF/TOF system in positive ion mode using either 2,5-dihydroxybenzoic acid or α-cyano-4-hydroxycinnamic acid as the desorption matrix. UV-Vis absorption spectra was performed on a Thermo Genesys 10S UV–Vis spectrometer. Fluorescence emission spectra was recorded on a Hitachi F-2500 spectrometer. GC–MS, HPLC was performed on a JASCO instrument equipped with a MD-2015 PLUS photodiode array detector, covering the wavelengths from 200-900 nm with an interval of 1.5 nm. The HPLC analysis was conducted at 25 °C using Dr. Maisch Reprosil 100-Si column (250 x 4.6 mm, normal phase with 5 um porous spherical silica). A solvent mixture of hexane (97%) and isopropanol (3%) was used as a mobile phase and the flow rate was maintained at 1.0 cm^3/min. Photolysis of the ester conjugates were carried out by using light-emitting diodes (LED) at 365 nm and an output power of 10-watt.

4.2 Synthesis of the click cluster C-I*G*$_1$. An anhydrous CH_2Cl_2 solution of compound **1** (87.7 mg, 0.13 mmol), Boc-protected I*G*$_1$ (76.2 mg, 0.16 mmol), and CuBr (22.8 mg, 0.16 mmol) was vigorously stirred at room temperature until the complete disappearance of compound **1**. The resulting solution was then extracted with CH_2Cl_2; the organic phase was washed with aqueous ammonia solution to remove copper catalyst and then dried over magnesium sulfate. Rotatory evaporating to dryness yields the Boc-protected click clusters C-I*G*$_1$ without further purification (96%). Boc-deprotection is readily carried out by acid-promoted hydrolysis. Trifluoroacetic acid (0.14 mL, 1.9 mmol) was added dropwise into an anhydrous CH_2Cl_2 solution of Boc-protected C-I*G*$_1$ (51.6 mg, 45 μmol). The mixture was then stirred under room temperature for 3 days, and the volatiles were removed under reduced pressure. The mixture was rinsed with hexane repetitively to remove excess acid, and then freeze-drying afforded amphiphilic dendron C-I*G*$_1$ as yellowish fluffy powders (97%). For Boc-protected C-I*G*$_1$, ^{1}H-NMR (400 MHz, $CDCl_3$): δ = 8.20 (bs, 1H), 7.78 (s, 1H), 7.43 (d, 1H), 6.86 (d, 1H), 6.81 (s, 1H), 6.40 (s, 1H), 5.42 (m, 1H), 5.29 (s, 2H), 5.01 (bs, 2H), 4.79 (t, 2H), 4.54-4.58 (m, 1H), 4.51 (d, 2H), 4.43 (t, 2H), 3.05-3.10 (m, 4H), 2.64 (t, 2H), 2.38-2.44 (m, 7H), 2.32 (t, 2H), 0.85-2.04 (m, 60H), 0.68 (s, 3H). For C-I*G*$_1$, ^{1}H-NMR (400 MHz, CD_3OD): δ = 8.17 (s, 1H), 7.60 (d, 1H), 6.98 (d, 1H), 6.91 (s, 1H), 6.28 (s, 1H), 5.42 (s, 1H), 5.37 (s, 2H), 4.39-4.57 (m, 5H), 3.52 (s, 2H), 3.06 (s, 6H), 2.80 (s, 2H), 2.41 (s, 2H), 2.15 (s, 4H), 0.86-2.07 (m, 38H), 0.70 (s, 3H); MALDI-TOF-MS: Cacld. For $(M+H)^+$ $C_{52}H_{80}N_7O_7$: 914.61 Da; Found: 914.28 Da.

4.3 Nile-red solubilization assay. Nile red stock solution (2.5 mM) was prepared in ethanol, and a dendron stock solution was prepared in PBS buffer at various concentrations depending on the starting concentration for the assay. Aliquots of the stock solution were taken and diluted with PBS to the desired concentration in a 1 mL assay volume. Nile red (1 μL) was added and the fluorescence emission was measured on a spectrofluorometer using an excitation wavelength of 550 nm. Fluorescence intensity was recorded at 635 nm. The photolytic reaction for the single molecule and the micelles in the solutions was performed by irradiating the sample solutions prepared in a quartz cuvette (1 cm x 1 cm) under a 365-nm LED. The distance between the sample and light source was kept at approximately 3 cm, and then the exposed solutions were analyzed by UV-vis and fluorescence spectroscopy.

4.4 Preparation of the Langmuir monolayers. A computer-controlled Langmuir trough (364 mm x 75 mm, KN2002 KSVNIMA) equipped with a Wilhelmy plate for surface pressure measurement was used obtain the surface pressure-area per molecule (π-A) isotherms. A monolayer at the air/water interface in the trough can be symmetrically compressed with two Teflon barriers at a given rate. Before each run, the trough was first filled with Millipore (18.2 MΩ cm) water as the subphase, and the surface pressure of the air/water interface was then zeroed. A chloroform solution of the compounds was then spread at the interface, and a period was allowed for solvent evaporation and for the system equilibrium. The monolayer was continuously compressed at a rate of 5 mm^2/min to record π-A isotherms with in situ fluorescence microscope observation (Axioskop, Carl Zeiss). The Nile red dye was selected the fluorescence probe for monitoring the assembly process at the

interface. The excitation/emission wavelengths were selected by an appropriate beam splitter/filter combination for the probes, and the monolayer was observed by using 50-fold magnification of an objective lens. For the photolytic reaction occurred at the air/water interface, the monolayer formed at a certain surface pressure and molecular area, maintained by keeping the barriers constant, was exposed to 365-nm LED irradiation. The change of the surface pressure with irradiation time was then recorded.

4.5 Contact angle measurement for the Langmuir-Boldgett films. The monolayer at surface pressure of 40 mN/m was transferred to a cover glass (2 cm x 2 cm) through a Langmuir-Blodgett (LB) deposition technique in a vertical dipping trough. The glass substrate was pre-rinsed with a piranha solution to yield a clean hydrophilic surface, and the LB film was fabricated by repetitive "up-down-up" strokes with a speed of 2 mm/min to form a sandwich structure composed of three molecular layers of the amphiphilic dendorn. The static contact angle for a water drop on thus-prepared LB film was then measured by a contact angle meter (CAM120, Creating Nano Technologies).

4.6 Fluorescence titration experiment. The titration experiments were carried out by fixing the concentration of fluorescence indicator C-IG_1 (1.5 x 10^{-9} mol) and varying the addition amount of DNA. The excitation and emission wavelengths was 320 nm and 390 nm, respectively, based on the intrinsic fluorescence feature for the coumarin moiety. The Stern-Volmer equation is utilized for the fluorescence quenching data process:

$$\frac{F_0}{F} = 1 + K[Q]$$

Where F_0 and F are the emission intensities in the absence and presence of quencher, K is a static quenching constant, and [Q] is the concentration of DNA.

4.7 EtBr displacement assay. 0.5 mL of pEGFP-C1 solution (1 μg/mL) and 7 μL of EtBr solution (0.1 mg/mL) were mixed thoroughly in PBS buffer, followed by adding 8 μL of the dendron solutions to the desired N/P values. EtBr in ultrapure water was measured as the background fluorescence of EtBr, and the solution that only contains pEGFP-C1 and EtBr in 1:1 binding ratio corresponds to the N/P = 0 with maximum emission intensity. The fluorescence emission was measured on a spectrofluorometer using an excitation of 540 nm, and the emission spectra were recorded from 540 nm to 700 nm.

REFERENCES

(1) Olejniczak, J.; Carling, C.-J.; Almutairi, A. *J. Controlled Release* **2015**, *219*, 18.

(2) Gangopadhyay, M.; Mukhopadhyay, S. K.; Karthik, S.; Barman, S.; Pradeep Singh, N. D. *MedChemComm* **2015**, *6*, 769.

(3) Barman, S.; Mukhopadhyay, S. K.; Gangopadhyay, M.; Biswas, S.; Dey, S.; Singh, N. D. P. *J. Mater. Chem. B* **2015**, *3*, 3490.

(4) Furuta, T.; Wang, S. S. H.; Dantzker, J. L.; Dore, T. M.; Bybee, W. J.; Callaway, E. M.; Denk, W.; Tsien, R. Y. *Proceedings of the National Academy of Sciences of the United States of America* **1999**, *96*, 1193.

(5) Lin, Q.; Bao, C.; Fan, G.; Cheng, S.; Liu, H.; Liu, Z.; Zhu, L. *J. Mater. Chem.* **2012**, *22*, 6680.

(6) Eckardt, T.; Hagen, V.; Schade, B.; Schmidt, R.; Schweitzer, C.; Bendig, J. *J. Org. Chem.* **2002**, *67*, 703.

成果報告 2

Title: Near-infrared-triggered photodynamic therapy toward tumorspheroidal human breast cancer cells using dendrimer-functionalized upconversion nanoparticles

1. Introduction

Recently, the biomedical applications of lanthanide-doped upconversion nanoparticles (UCNPs) have attracted much attention [1-6]. Because UCNP-based materials can sequentially absorb two or more photons, they exhibit a unique anti-Stokes shift of fluorescence emission in UV–visible wavelengths (300–700 nm) under NIR light excitation (750–1400 nm). The unique "photon upconversion" process has several merits, including reduced fluorescence background, improved tissue penetration, and lower phototoxicity in biological fields [7]. Moreover, UCNPs usually exhibit multiple fluorescence emission bands of UV, blue–green, and red light simultaneously under NIR excitation. Additionally, finely manipulating the doped-metal composition or the host crystal structure can lead to specific upconverted emissive patterns. For example, the nanoparticles doped with erbium (Er^{3+}) instead of thulium (Tm^{3+}) can switch emission wavelengths from blue to green light as well as enhance red-light intensity; a single band, intense red-light emission is achieved by incorporating manganese (Mn^{2+}), ytterbium (Yb^{3+}), and Er^{3+} into the nanostructure [8-10]. Combined with the robust, well-developed synthetic protocols, UCNPs bearing specific upconverted emission profiles are promising for photo-assisted cancer treatments, particularly photodynamic therapy (PDT) [11-14].

PDT based on the photochemical reactions of photosensitizers (PSs) is a treatment strategy involving light irradiation at appropriate wavelengths, by which PS molecules can produce cytotoxic reactive oxygen species (ROS) and singlet oxygen ($^1O_2$) to destroy nearby cancer cells [15]. The greatest advantage of PDT is the ability to selectively treat tumor cells by using light under spatiotemporal control. However, most PS molecules are excited by visible or UV light, which have poor tissue penetration, thus limiting the treatment of large or internal tumors. Loading the PS molecules onto the UCNPs surface avoids this drawback, as it facilitates NIR-triggered PDT, which is based on upconverted fluorescence emission and resonance energy transfer. Several strategies have been developed to immobilize the PS molecules on the surface including mesoporous silica coating and polymer encapsulation [9, 16-19]. Intense upconverted emission at suitable wavelengths and higher loading capacity of the active molecules was proposed for guaranteeing more effective therapeutic outcomes. Liu and coworkers demonstrated a layer-by-layer (LBL) method for loading multiple layers of PS-conjugated polymers onto the surface of UCNPs surface through electrostatic interaction [13]. Both in-vitro and in-vivo PDT effects were substantially improved through their multiloading strategy. As clinical PDT develops, fabricating PS-conjugated-UCNP systems with commercialization potential by using more facile and robust synthetic protocols remains challenging.

This paper introduces the application of dendrimers in the encapsulation layers of UCNPs for trapping PS molecules according to the multivalency of the dendritic structures [20]. Dendrimers, well-defined hyperbranched polymers consisting of a central core, radiating branches ending in multivalent terminal groups, and cavities within the branched structure have aroused much interest in the past two decades [21-24]. For example, a full-generation poly (amido amine) (PAMAM) dendrimers bear multiple primary amines on the surface and internal tertiary amines as branching sites. These tertiary amines can be protonated to generate polycations at physiological pH, thus allowing for electrostatic interaction and subsequent formation of complexes with molecules bearing opposite charges [25-28]. Apart from electrostatic binding, the internal cavities within the dendrimers can accommodate small molecules through host–guest affinity. Accordingly, typical fourth-generation PAMAM dendrimers (G4), bearing 64 peripheral amines, were immobilized on the surface by using the facile LBL strategy to create positively charged UCNPs. The material design enhanced the cellular uptake of the nanoparticles as well as the absorption of negatively charged PS molecules by those dendrimers (Fig. 1). A 980-nm NIR laser diode (LD) was used as the light excitation source to

analyze upconversion and the in vitro PDT effect. Moreover, the $^1O_2$ production combined with the apoptosis of human breast cancer cells of MCF-7 lines cultured in two-dimensional (2D) arrays and three-dimensional (3D) spheres was explored to elucidate the NIR-triggered PDT efficacy in different cell models [29, 30].

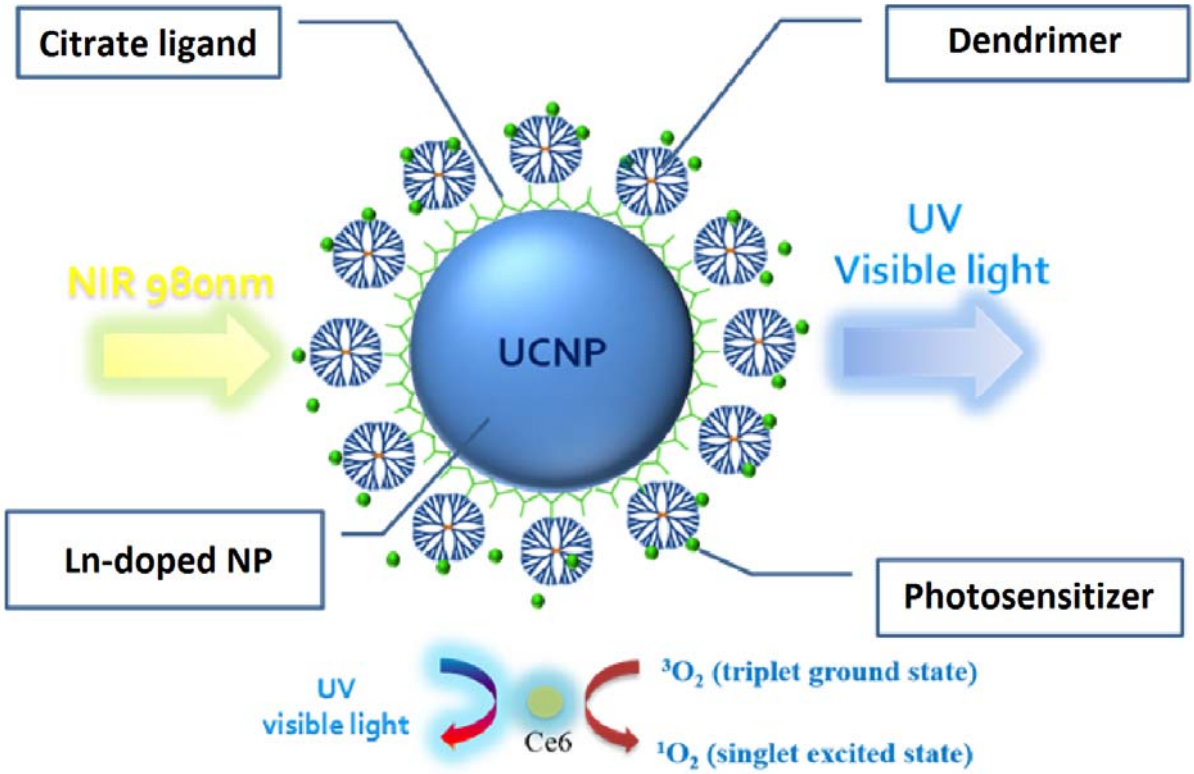

Fig. 1. NIR-light-triggered photodynamic therapy based on a lanthanide-doped $NaYF_4$ upconversion nanoparticle (UCNP) sequentially encapsulated with citrates, PAMAM dendrimers, and chlorin e6 (Ce6) via a layer-by-layer (LBL) absorption method.

2. Results and Discussion

Preparation of Lanthanide-doped UCNPs. Yb^{3+}- and Tm^{3+}-doped $NaYF_4$ nanocrystals were used as core materials in the NIR-induced PDT because of their high efficacy in NIR-to-visible light upconversions. Herein, chlorin e6 (Ce6), a chlorophyll analog with significant absorption, maximum at approximately 400 nm (Soret band) and 660 nm (Q band), was used as the PS in the PDT investigation at the cellular level [31, 32]. The UCNPs were synthesized using a solvothermal procedure at 300 ºC with oleic acid (OA) as the stabilizer [33]. To enhance the energy transfer between the doped ions and host materials, the core of the UCNPs was further covered by a layer of undoped $NaYF_4$ to form a core shell [34]. The crystallinity and composition for the UCNPs were characterized using XRD and EDXS, suggesting α–phase (cubic–like) $NaYF_4$ with successful Yb^{3+} and Tm^{3+} doping (see the SI, Fig. S1 and S2). As shown in Fig. 2a, the images of the core-shell nanocrystals, taken using TEM, display a polygonal morphology with an average dimension of 16.0±2.1 nm. Moreover, a cubic-like nanocrystal larger than 50 nm was clearly observed in certain grid areas, which is consistent with the XRD data (Fig. 2b). As shown in Fig. 2c, the prepared UCNPs emitted upconverted fluorescence at multiple bands of UV (λ_{max} = 360 nm), blue (λ_{max} = 480 nm), red (λ_{max} = 650 nm), and NIR (λ_{max} = 795 nm) wavelengths under 980 nm LD excitation. Notably, the fluorescence intensity was considerably increased by the core-shell strategy. Among the bands, the UV and red emissions are capable of exciting the Ce6 that possesses corresponding absorption, and more intense blue and NIR emissions allow for tracing the biodistribution of the UCNPs through fluorescence microscopy.

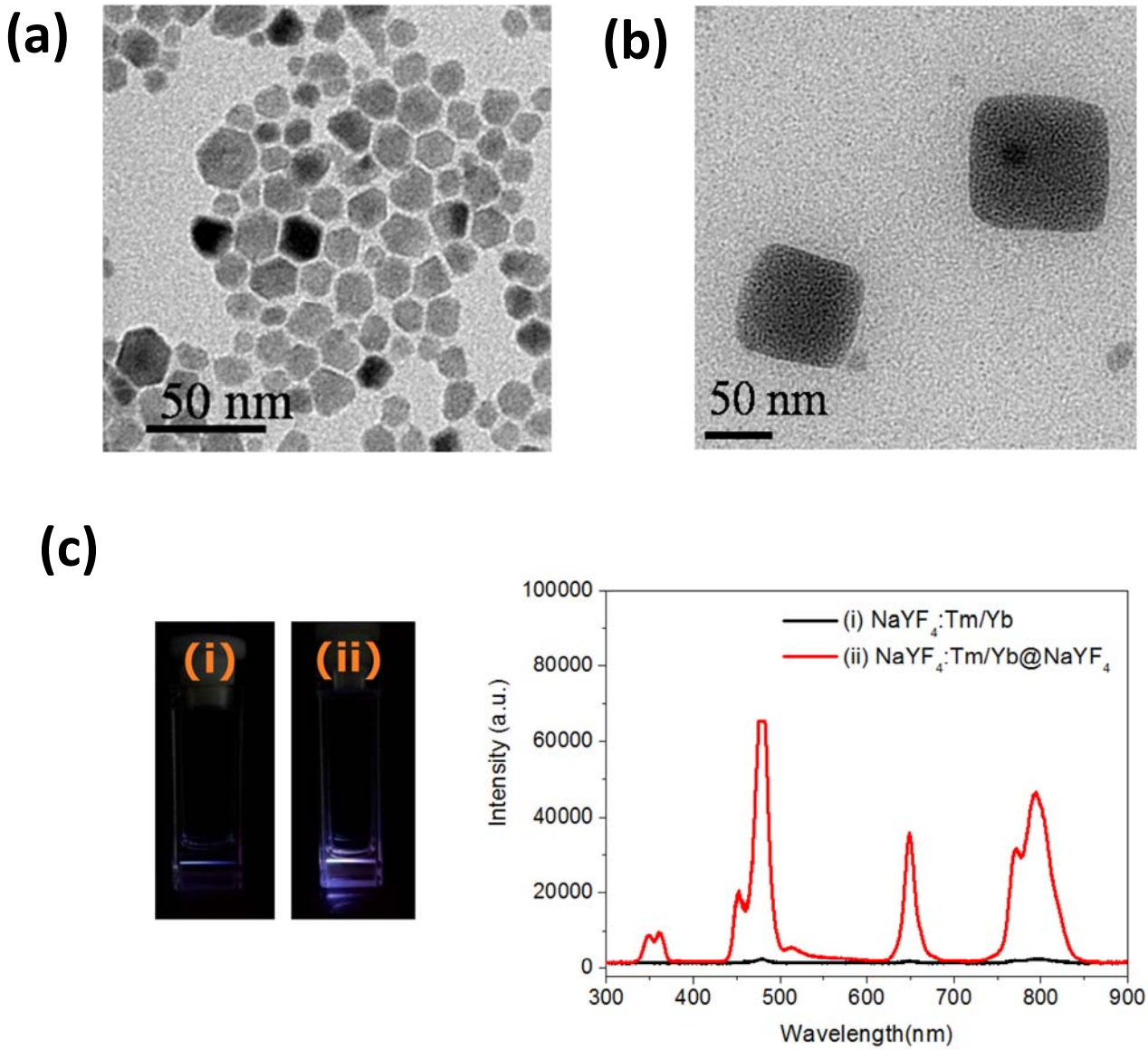

Fig. 2. Transmittance electron microscopic (TEM) images of (a) polygonal (small) and (b) cubic-like (large) $NaYF_4$ nanocrystals. The average dimension for (a) was calculated based on 100 nanoparticles selected from a TEM micrograph. (c) Upconversion fluorescence spectra of the (i) core and (ii) core-shell nanocrystals under 980-nm laser excitation. The spectra recorded by a CCD imaging spectrometer exhibits UV, blue, red, and NIR wavelengths simultaneously.

Fabrication of UCNPs through Ligand Exchange and the LBL Strategy. Synthetic strategies involving the encapsulation of mesoporous silica and water-soluble polymers have been developed for preparing the hydrophilic UCNPs used in biomedicinal applications. To fabricate the nanoparticle surface with polycationic G4 in this hybrid system, negatively charged UCNPs are produced and, the dendrimers are electrostatically adsorbed using the LBL method.[13] The first attempt of using an ozonolysis reaction to cleave the double bonds of the oleate ligands for generating anionic carboxylate groups was unsuccessful, because the oxidative treatment under acidic condition led to the unexpected desorption of the surface ligands [35]. The removal of the ligands was confirmed by TGA measurement (see the SI, Fig. S3) [12]. Alternatively, the oleate ligands were readily exchanged by a trivalent ligand of sodium citrate in diethylene glycol under 200 ºC, thus allowing for the fabrication of the UCNPs with multiple carboxylate groups as the first layer [36]. The NH_2-determinated G4 dendrimers on the UCNPs were then immobilized through electrostatic interaction at ambient temperature, thus generating water-dispersible nanoparticles with excess positive charges on the surface and forming the second layer. After the exchange with the citrate ligands, the zeta potentials of the modified UCNPs revealed a negatively charged surface ($\zeta = -8.54$ mV), however, a positive charge ($\zeta = +31.7$ mV) presented after the dendrimer encapsulation (see the SI, Fig. S4). Moreover, FT-IR analysis confirmed the exchanged citrate ligands through the characteristic carboxylate stretching at 1586 and 1400 cm^{-1}, and the featured amide stretching of the PAMAM dendrimers adsorbed on the surface was well characterized at 1640 and 1560 cm^{-1} (see the SI, Fig. S5). As illustrated by the TEM images shown in Fig. 3a and 3b, the morphology and dimensions of the UCNPs were mostly unaltered after citrate and dendrimer modification, but the boundary of each dendrimer-encapsulated nanoparticle was less defined. This observation was presumably because of the strengthened interactions between the nanoparticles including the hydrogen bonding and van der Waals force produced by the G4 PAMAM dendrimers. Moreover, the hydrodynamic dimension of the G4-functionalized UCNPs determined by dynamic light scattering is approximately 180 nm with a narrow distribution, suggesting that these dendrimers were successfully immobilized on the surfaces of the UCNPs (see the SI, Fig. S6). Although the dendrimer interaction may have led to substantial aggregation in these water-dispersible UCNPs, the upconversion emission still exhibited distinct fluorescence bands in the UV-, blue-, and red-light regions (Fig. 3c).

The organic contents of the modified UCNPs were calculated using the weight-loss data obtained through TGA, and approximately 15% and 25% of the oleate and citrate ligands, respectively, were immobilized on the UCNP surface (see the SI, Fig. S3). Assuming that 1) every UCNP exhibited a spherical shape and uniform size upon TEM analysis, and 2) the mass of a nanoparticle is calculated from the bulk density of $NaYF_4$ (4.21 g/cm^3), the ligand density per particle can be determined using the simple calculation proposed by Winnik and coworkers [37]. The coverage densities of oleate- and citrate-modified UCNPs, were 4.8 and 11 ligands/nm^2, respectively; thus, approximately 4000 oleate and 9000 citrate molecules covered each nanoparticle. Moreover, by finely adjusting the feeding concentration of dendrimers to UCNPs, approximately 60 dendrimers were delivered to one citrate-modified UCNP. Based on Winnik et al.'s calculation, one polycationic G4 dendrimer was theoretically accommodated by 150 polyanioinic citrate molecules. Accordingly, the dendrimers could be firmly immobilized on the UCNP surface through multivalent interactions.

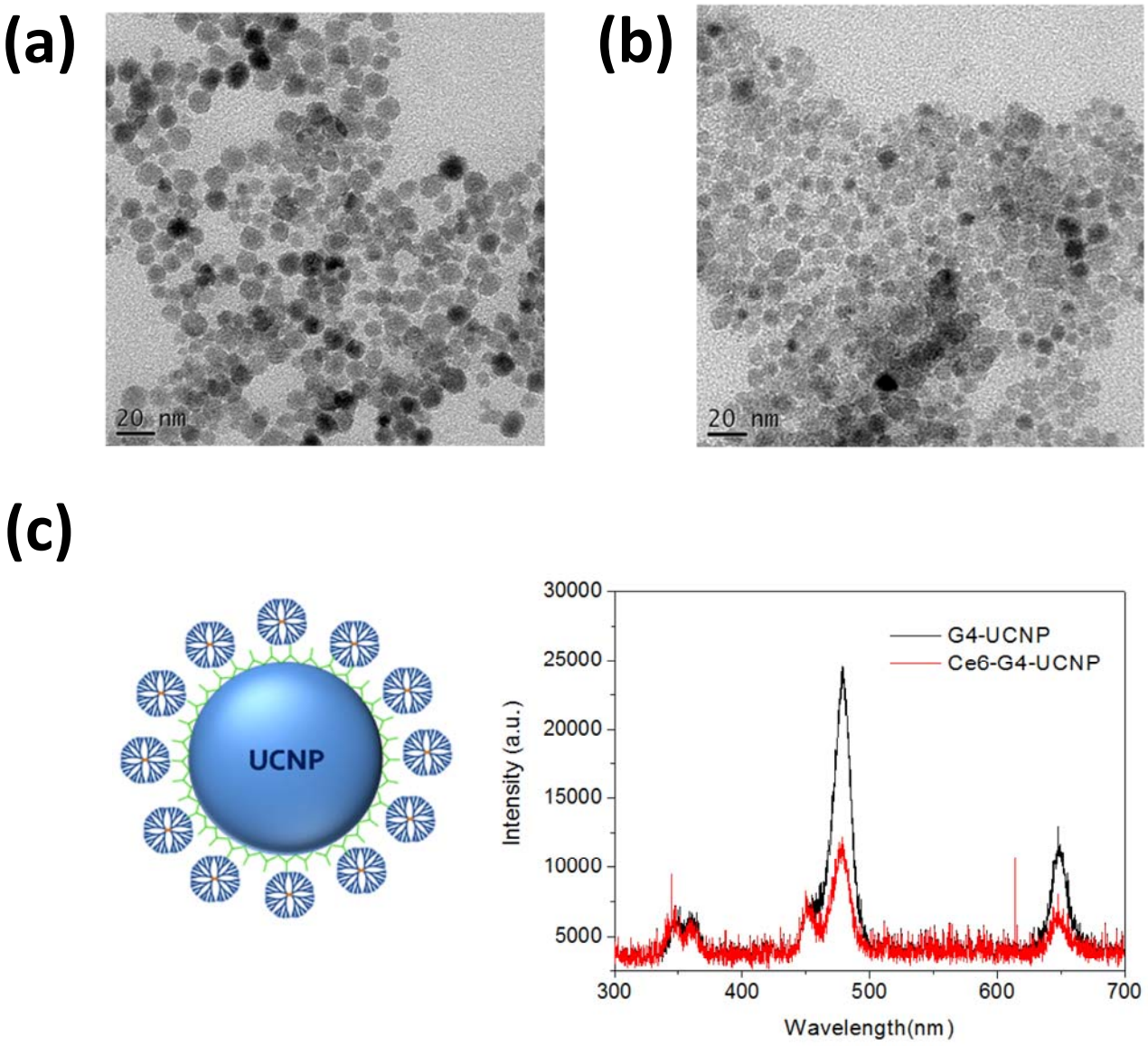

Fig. 3. Transmittance electron microscopic (TEM) images of (a) citrate and (b) PAMAM dendrimer-encapsulated nanoparticles (G4-UCNP). (c) Upconversion fluorescence of G4-UCNP in water under 980-nm laser excitation. The fluorescence intensity was extinguished after encapsulation of Ce6 (Ce6-G4-UCNP).

The negatively charged Ce6 molecules were then directly loaded onto the dendrimer-encapsulated UCNPs to form the third layer through the electrostatic binding of the COOH and NH_2 groups. The zeta potential of the hybrid UCNPs decreased from +31.7 to +24.0 mV, suggesting that negatively charged Ce6 molecules covered the surface of the nanoparticles and thus partially neutralized the cationic density produced by the dendrimers (see the SI, Fig. S4). Moreover, as shown in Fig. 4a, the UV–vis spectrum also confirmed the Ce6 adsorption through the characteristic Soret and Q-band absorption bands at 407 and 643 nm, respectively. Notably, the Q band of the hybrid UCNPs exhibited substantial blue-shifted wavelength compared with that of free Ce6, which suggests that the PS molecules were entrapped by the surface dendrimers. Generally, the interior cavities of PAMAM dendrimers possess a hydrophobic domain. Once chromophores or fluorophores are trapped inside the dendritic cavities, their absorption or emission wavelength shifts hypsochromically in contrast to the free probe molecule in aqueous solution [38]. Therefore, the red fluorescence emission of the water-immersed hybrid UCNPs under the excitation of the Soret band was also blue shifted by approximately 20 nm (Fig. 4b). In addition, the loading capacity of the Ce6 molecules could be readily determined based on the fluorescence intensity of the nonadsorbed Ce6 that washed off of the hybrid UCNPs. The loading amount increased with the initial feeding concentration of the Ce6. This was due to the multivalent character of the dendrimers, assisting the adsorption of the PS molecules through the exterior and interior interactions caused by electrostatic and host–guest affinity, respectively. Fig. 4b also shows a blue-to-green fluorescence band (430–580 nm), which is presumably attributable to the intrinsic emission of the G4 dendrimer [28, 39, 40]. Notably, the fluorescence intensity of the G4 decreased with increasing Ce6 content. This result implies a strong interaction between the dendrimer and the entrapped Ce6, because the emission of the dendrimer and the absorption of the Ce6 occupied proximal wavelength regions, thus facilitating the fluorescence energy transfer. Moreover, this result clearly indicates that the PS molecules were firmly immobilized by the PAMAM dendrimers on the surfaces of the UCNPs. Fig. 3c depicts the upconversion fluorescence spectra of the aqueous hybrid UCNPs under NIR-laser excitation. The emission wavelengths centered at the UV-, blue-, and red-light regions were unaltered after the surface modification. However, the visible-light emissions of the UCNPs were extinguished by the peripheral Ce6, principally through the Soret and Q-band absorptions, a manifestation of effective energy transfer from the UCNPs to the surrounding PS molecules [41-43]. Notably, even the weak absorption band of the Ce6 (Fig. 4a) at approximately 480–520 nm demonstrated substantial absorption of the blue fluorescence emitted from the UCNPs. Finally, the PS molecules were successfully photoexcited by the 980-nm NIR laser, using the dendrimer-encapsulated UCNPs as the nanoplatform.

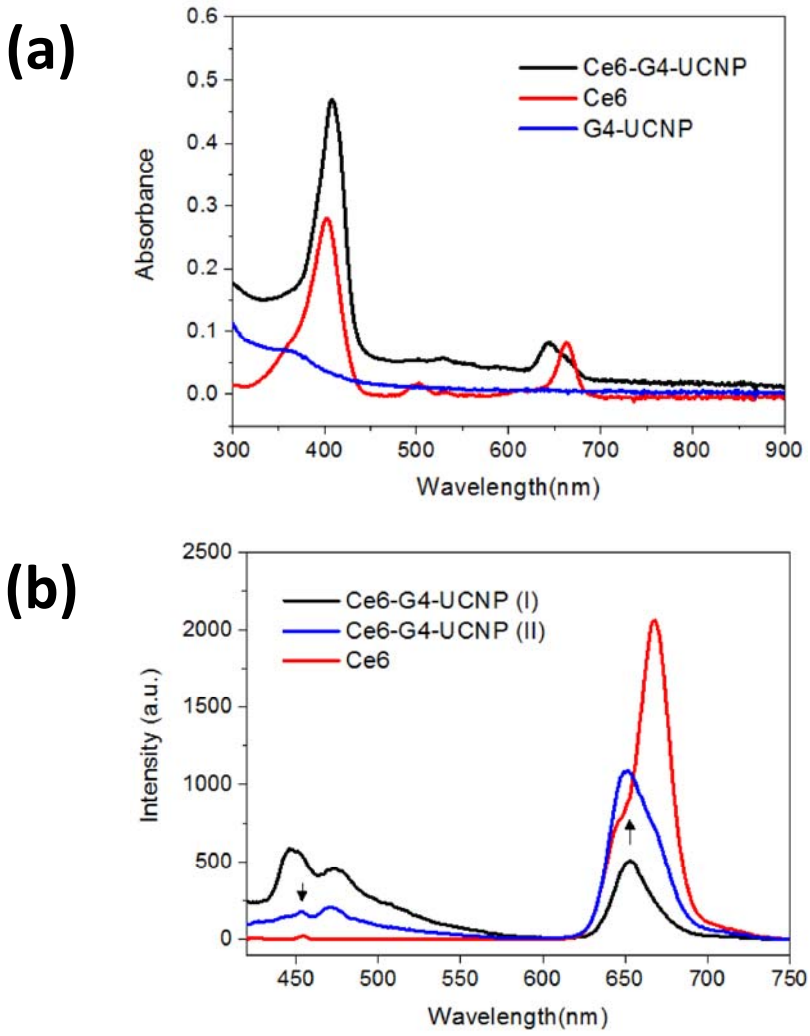

Fig. 4. (a) UV-vis absorption and (b) fluorescence spectra of the hybrid nanoparticles sequentially encapsulated with dendrimers (G4-UCNP) and Ce6 (Ce6-G4-UCNP) in comparison with that of pristine Ce6; (I) and (II) denote different loading capacity of Ce6.

The Evaluation of Photoactivity and Singlet Oxygen ($^1O_2$) Formation. To assess the capability of the hybrid UCNPs to generate $^1O_2$, a fluoresceinyl Cypridina luciferin analogue (FCLA) was employed as a chemiluminescence probe [14]. The FCLA was oxidized by $^1O_2$ and thus markedly enhanced fluorescence by 524 nm. Fig. 5a and 5b illustrate the correlation of the laser irradiation time and fluorescence intensities of FCLA in the presence of PSs. The Ce6 and hybrid UCNPs exhibited fluorescence intensities of approximately two-and-a-third-fold and three-and-a half-fold increments, respectively, and plateaued upon 660-nm laser irradiation for 16 min, by which the Ce6 molecules were directly photoexcited through the Q-band absorption. The FCLA assay could detect the accumulation of the $^1O_2$ in water by increasing the exposure time of the red light. Notably, the hybrid UCNPs were also sensitive to the irradiation using a 980-nm NIR laser, displaying a two-fold increase in fluorescence; whereas, the Ce6 was completely unreactive to the NIR light. This result clearly confirmed that the Ce6 immobilized by the dendrimers was photoexcited by the upconverted fluorescence emitted from the UCNPs nanoplatform. Moreover, as shown in Fig. 5c, the UCNPs with a higher loading of Ce6 generated substantial $^1O_2$ under 980-nm laser irradiation, attributed to the merits of using the polyvalent dendrimers as the adsorption layer to accommodate more PS molecules through both exterior and interior interactions. Considering all the assay data, the photoactivation permitted energy transfer between the excited Ce6 and surrounding oxygen molecules, generating significant $^1O_2$ as the major ROS in NIR-light-triggered PDT for solid tumors.

In Vitro PDT Analysis for Human-Breast Cancer Cells. Laser-triggered PDT was performed on the MCF-7 cell lines that were cultured in the 2D and 3D models [44, 45]. Generally, 2D cell-culture systems are a convenient way to study cancer cells in vitro; however, tissue-specific architecture with cell–cell and cell–extracellular matrix interactions are reduced when cells grow on flat and adherent substrates. Solid tumors growing in a 3D spatial conformation are currently being developed as more advanced in vitro models. A key advantage of 3D cultures in preclinical research is their capacity to modulate the molecular gradients that exist in living tissues, such as oxygen, nutrients, metabolites, and signaling molecules. Hence, 3D models mimic the complexity of tissues more precisely than conventional 2D monolayers, thus potentially bridging the gap between 2D cultures and animal models. Moreover, cells cultured in a 3D scaffold generate a cell population by enhancing the properties of cancer stem cells (CSCs), which have been demonstrated to retain cancer-initiating potential and self-renewal capability and lead to tumorigenesis and drug resistance in malignant tumors in vivo. In addition, 3D cell cultures usually upregulate the expression of hypoxia-responsive genes and are thus more resistant to PDT than 2D monolayers, because of limited oxygen supply in the 3D spheroids. Accordingly, performing NIR-triggered PDT in a 3D model of the MCF-7 CSCs using the hybrid UCNPs as the PS is a therapeutic challenge.

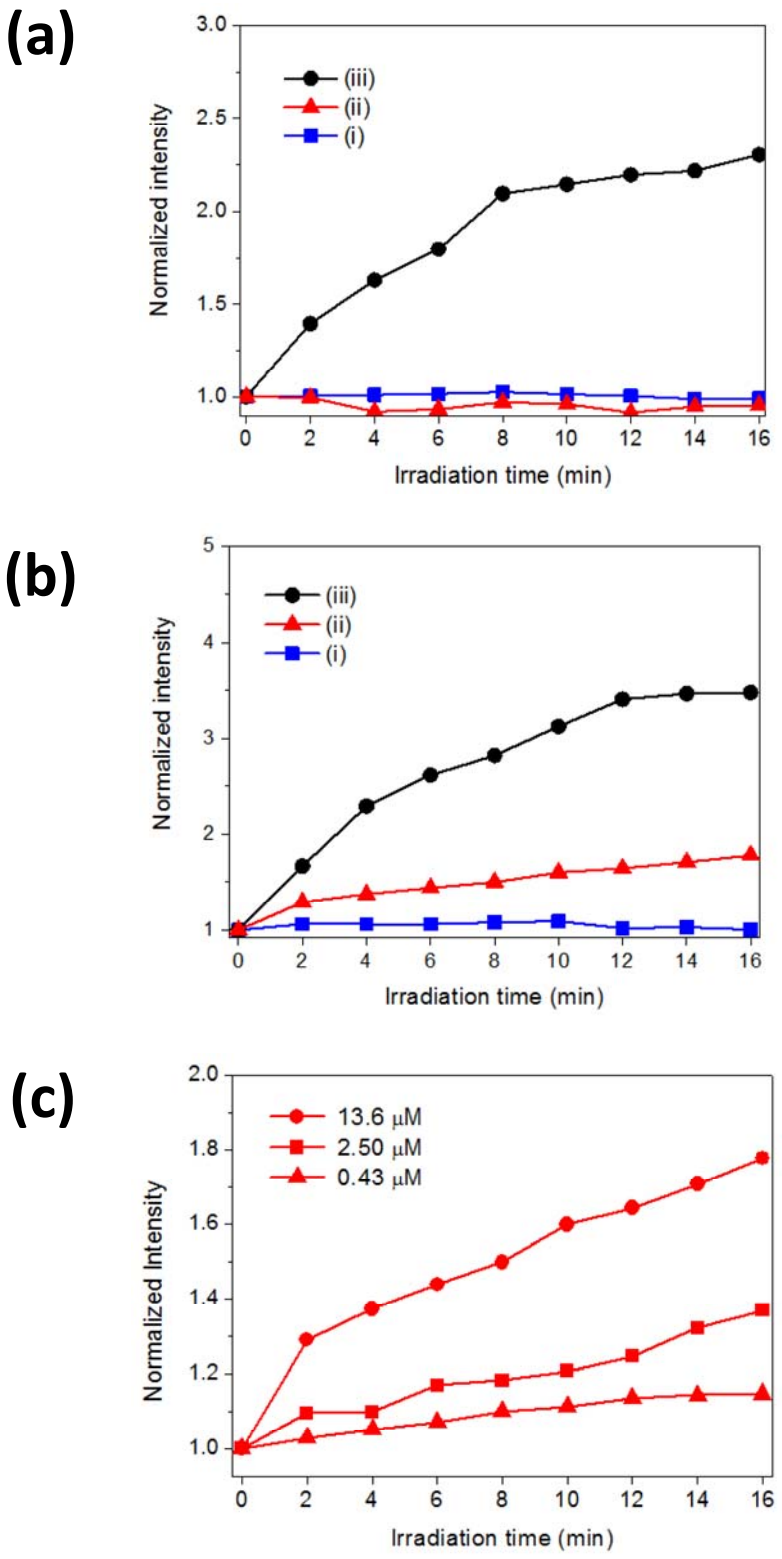

Fig. 5. The FCLA assay for determining the accumulation of singlet oxygen using (a) pristine Ce6 and (b) hybrid nanoparticles (Ce6-G4-UCNP) as the photosensitizer; (i) dark condition, (ii) 980, and (iii) 660-nm laser excitation. (c) The Ce6-G4-UCNP with increasing loading capacity of Ce6 (0.43, 2.50, and 13.6 M) under 980-nm laser excitation. The fluorescence intensity was normalized to the intrinsic fluorescence of FCLA solution in the absence of additives and light exposure.

Under darkness, Ce6 was nontoxic for the MCF-7 cells cultured in a conventional 2D system at a high dose (10 μM), but it immediately became a chemotherapy drug and completely destroyed target cells under 660-nm laser excitation for 10 min, which potentially favored photodynamic medication under spatiotemporal control. However, the PDT outcome was ineffective when the 980-nm NIR laser was used as the excitation source, because the Ce6 was nearly transparent at this wavelength and photoinduced $^1O_2$ production was inhibited. The median lethal dose of Ce6 for the MCF-7 cells under 660-nm laser irradiation was below 1 μM, suggesting that Ce6 is an effective PS responsive to the red light.

Fig. 6 presents the survival test results for the 2D cell cultures, using the hybrid UCNPs as the PS under laser excitation. Herein, the loading concentration of the Ce6 on the UCNP determined through fluorescence spectroscopy was approximately 0.25 μM. The control experiments demonstrated that the hybrid UCNPs were also nontoxic in the dark and that 86% and 91% of the MCF-7 cells survived in the presence of pristine Ce6 under 660- and 980-nm laser irradiation, respectively. This result suggests that the PDT efficiency was quite low at this Ce6 dosage under laser excitation. In sharp contrast, when the Ce6 was loaded onto the dendrimer-modified UCNPs, approximately 50% of the cells died under 660-nm light. Compared with the Ce6, the hybrid UCNPs exhibited higher PDT performance, presumably because of higher cellular-uptake efficiency through endocytosis. Generally, the accumulation of Ce6 in target cells is inefficient because the negatively charged COOH groups may be electrostatically repulsed by the cell membranes; based on the surface PAMAM dendrimers, the hybrid UCNPs possess multiple positive charges, thus favoring the cellular uptake of the nanoparticles. Therefore, the accumulation of PS in the cells, using the UCNPs as the drug carrier, would be considerably enhanced under the same incubation time. Most crucially, approximately 70% of the cells were killed under 980-nm laser irradiation, indicating the PDT efficiency was increased under NIR light. FCLA analysis revealed that the hybrid UCNPs exposed to the 660-nm laser induced higher $^1O_2$ formation than the 980-nm laser did, because the photoexcitation of the Ce6 was less effective through the upconversion fluorescence emitted from the UCNPs (Fig. 5b). However, the in vitro PDT experiments demonstrated a contrary result; NIR-laser irradiation provides more positive therapeutic outcomes in MCF-7 cell lines. Because the polycationic UCNPs improved the cellular uptake, the marked NIR-triggered PDT effect was due to longer laser wavelength and thus deeper tissue penetration. Although higher $^1O_2$ was produced under red-light excitation in the tube test, NIR light could easily pass through the cell membrane and some organelles and reach the hybrid UCNPs. Therefore, surface Ce6 was effectively photoexcited under 980-nm laser irradiation, thus dramatically enhancing the overall PDT effect.

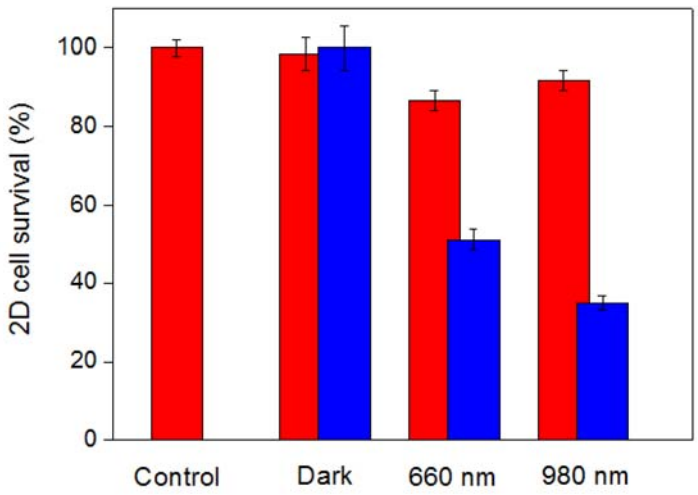

Fig. 6. Photo-induced cytotoxicity for MCF-7 cells cultured in a 2D system in the presence of pristine Ce6 (red) and hybrid nanoparticles (blue) as the photosensitizer under laser irradiation. [Ce6] = 0.25 μM.

The MCF-7 cells were also cultured on ultralow attachment surfaces in serum-free mediums with limited growth factors to form the 3D scaffolds. These tumorspheres, which have been proven to possess CSC-like properties, served as an effective in-vitro platform for screening anti-CSCs drugs. The 3D cells were also exposed to the 660- and 980-nm lasers to compare the wavelength-dependent PDT efficiencies. Immediately after exposure, live-dead staining was performed to evaluate viability distribution of the cells in tumorspheres [46]. Fig. 7a shows the pretreatment distribution of the living and dead cells in the 3D spheres specifically labeled with green and red fluorophores. Additionally, Fig. 7b demonstrates that after treating the cells with the hybrid UCNPs under darkness, the dead cells marked in red were mainly located at the peripheral of the 3D spheres. The natural apoptosis of the surrounding cells during the cultivation of the tumorspheres was the possible cause of this observation. When the treated 3D cells were exposed to the laser light, the dead portions were clearly located inside the spheres, indicating that the UCNPs successfully absorbed by the tumorshperes produced the PDT effect, not only at the surface but also at the center of spheres. Moreover, comparing Fig. 7c and 7d, we noticed that the 980-nm laser induced higher cell death inside the spheres. This result indicates that the NIR-light penetrated the 3D scaffolds more deeply, thus triggering the PDT outcome according to the accumulated hybrid UCNPs. Furthermore, as shown in Fig. 7e, the quantitative analysis was conducted by manually counting the live and dead cells, based on the spheres selected from the fluorescence images. The result was consistent with the survival test for 2D cells, confirming the highest PDT performance, the lowest percentage of cell survival under 980-nm laser irradiation. To our knowledge, this is the first example of NIR-light-driven PDT on a 3D tumorspherical platform using UCNPs as the PS, carrier, and activator, simultaneously.

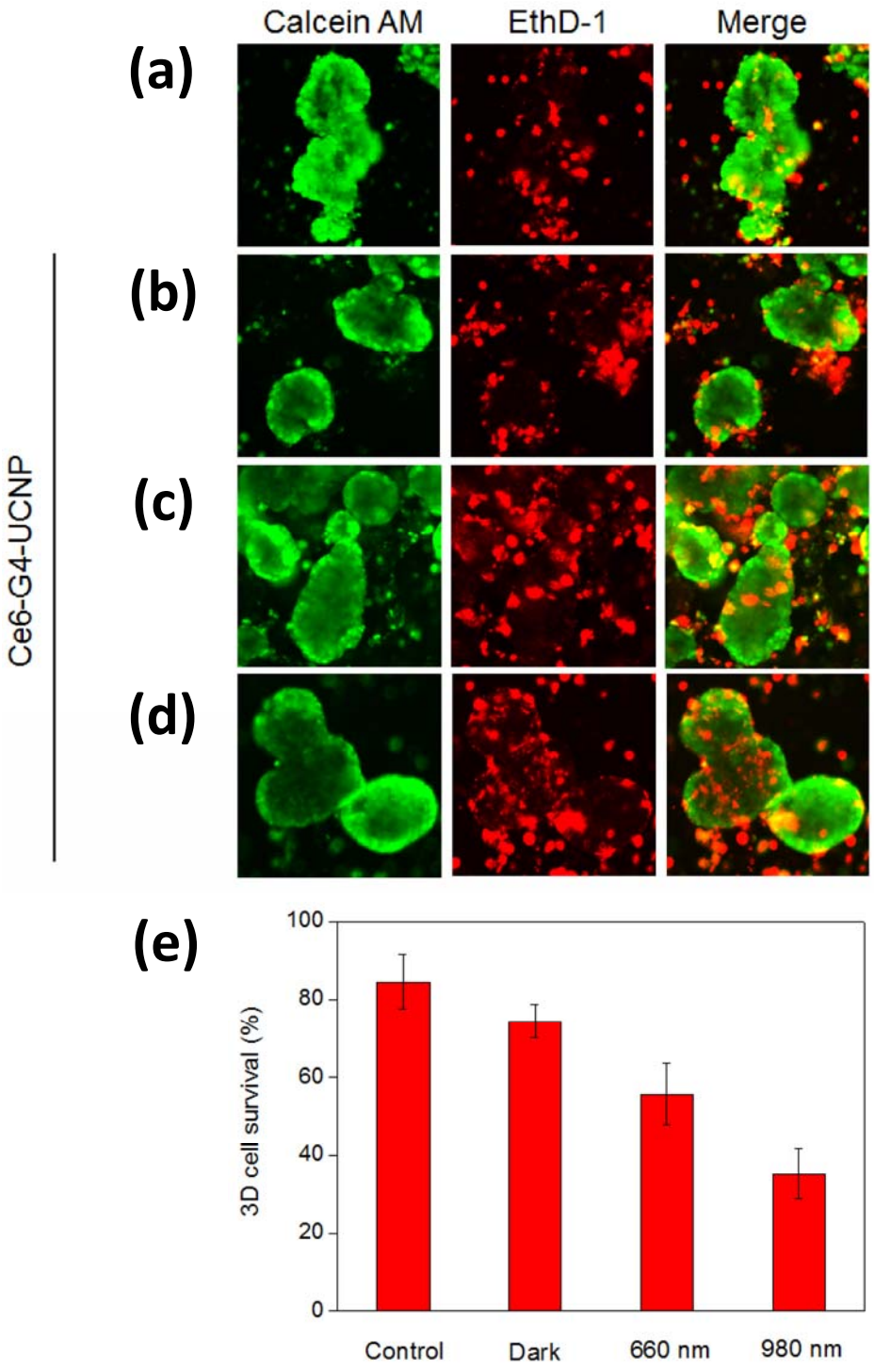

Fig. 7. Fluorescence staining images for MCF-7 cells cultured in a 3D tumorsphere system; (a) control: live (calcein AM, green) and dead (EthD-1, red) cells in the absence of hybrid nanoparticles and light exposure, (b)-(d) in the presence of hybrid nanoparticles in dark condition, under 660-, and 980-nm laser irradiation, respectively. (e) Quantitative analysis for the average distribution of live and dead cells in a tumorsphere with a standard deviation based on 10 spheres selected from the fluorescence images. [Ce6] = 0.25 μM.

Tumorspheres driven from cancer cells have been proven to display characteristics of CSCs, which are considered the main cause of cancer recurrence. Because the 3D spheres grow divergently, from the core to peripheral, the cells inside the spheres may exhibit more characteristic CSC/progenitor cell properties than the cells located on the surface. For the MCF-7 cells cultured in the 3D tumorspheres, the hybrid UCNPs combined with a NIR laser exhibited remarkable deep-tissue PDT effects, allowing for more effective destruction of the CSCs located inside the spheres. Moreover, the PDT outcome can be readily enhanced by increasing the dosage of hybrid UCNPs, light exposure time, and the power of the incident laser. Fig. 8 illustrates that the NIR-light-triggered PDT killed most of the cells in the tumorshperes when the exposure time was increased to 20 min under the treatment of the UCNPs with higher Ce6 loading (1.36 μM). Considering all aforementioned factors, hybrid UCNPs are promising NIR-triggered PDT modules for application in the treatment of spheroidal CSCs.

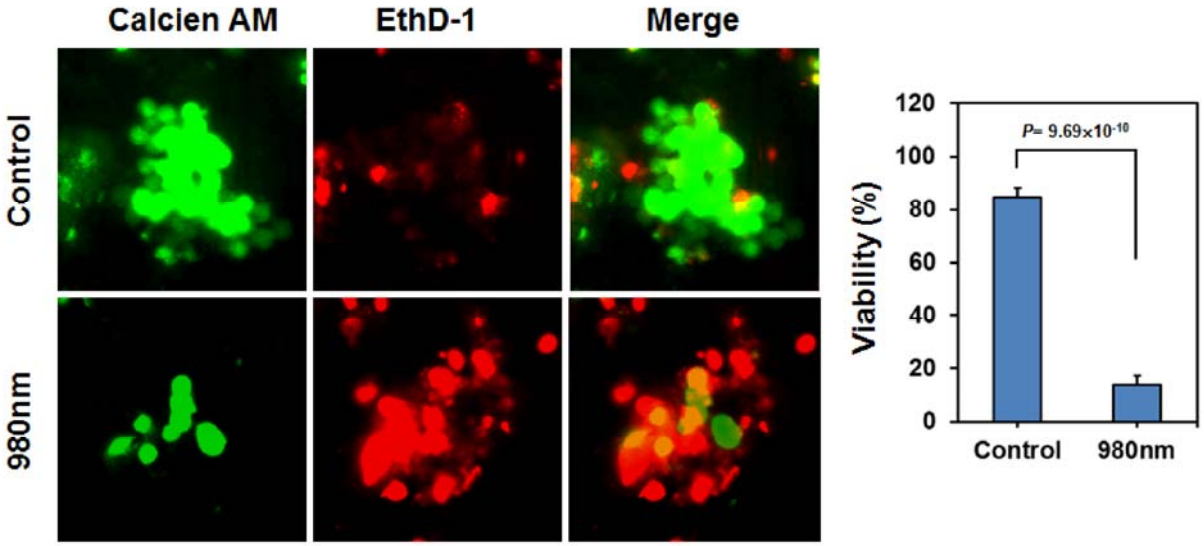

Fig. 8. Fluorescence staining images for live and dead MCF-7 cells in a tumorsphere in the presence of hybrid nanoparticles with higher loading capacity of Ce6 (1.36 μM). The quantitative analysis shows that less than 20% of cells were survived under 980-nm laser irradiation for 20 min.

3. Conclusion

We successfully synthesized hybrid UCNPs for performing NIR-light-driven PDT on human breast cancer MCF-7 cell lines. The water-soluble nanoparticles composed of lanthanide-doped $NaYF_4$ nanocrystals encapsulated by the PAMAM dendrimers exhibited significant upconversion fluorescence under 980-nm laser irradiation. Thereby, the Ce6 molecules immobilized on the surface through an LBL strategy were effectively photoexcited to generate cytotoxic ROS. The chemiluminescence assay confirmed that $^1O_2$ as the main ROS was readily accumulated during the photoexcitation and that the 660-nm LD was a more effective light source for photoexciting the hybrid UCNPs through the Q-band absorption of the Ce6; however, in-vitro experiments revealed that the 980-nm-laser light had higher cytotoxicity in the MCF-7 cells cultured according to a conventional 2D model. The reverse PDT outcome was apparently because the NIR light demonstrated higher penetration of a living system than visible light did. Moreover, compared with pristine Ce6 under visible-light excitation, the hybrid UCNPs displayed optimal in-vitro PDT efficacy under NIR-light excitation. This finding is attributed to the enhancement of cellular uptake by the polycationic dendrimers through electrostatic interactions with polyanionic membrane lipids. Most notably, NIR light also induced an efficient PDT effect in the 3D cell model of MCF-7 tumorspheres, suggesting that hybrid UCNPs can be effectively applied in more complicated cellular textures. Because tumorspheres have been proven to possess enhanced CSC-like properties, hybrid UCNPs can be a promising candidate for NIR-triggered PDT in the clinical treatment of CSCs.

4. Materials and methods

2.1 Materials and instruments

The chemical reagents and organic solvents for materials synthesis were obtained as high-purity reagent-grade from commercial suppliers and used without further purification. The fourth generation PAMAM dendrimer (G4-NH_2) was purchased from Dendritech, Inc. (MI, USA). For the materials analysis, FT-IR was performed on a Bruker Alpha FT spectrometer. UV-vis absorption spectra were recorded on a Thermo Genesys 10S UV-vis spectrometer equipped with a thermostatic cuvette holder. Fluorescence emission spectra for $^1O_2$ analysis was recorded on a Hitachi F-2500 spectrometer. TEM, EDXS, and XRD were performed on a Jeol JEM-2100 instrument, a Jeol JSM-6330F instrument, and a Bruker D2 PHASER X-ray Diffractometer, respectively. Dynamic light scattering analysis involving particle size and zeta potential measurements was carried out by a Malvern Zetasizer Nano ZS. TGA was recorded on a Thermo Cahn VersaTherm HS TG analyzer. The analysis for upconversion fluorescence and photodynamic reaction were carried out by a home-made experimental apparatus using either 660- or 980-nm laser diode as the excitation source (output power: 2 W). The upconversion emission from the samples in a cuvette folder was collected and induced by a fiber bundle into a CCD imaging spectrometer (USB-4000, Ocean Optics) for spectra recording.

2.2 Synthesis of hybrid UCNPs

$NaYF_4$:Yb,Tm/$NaYF_4$ UCNPs with a core-shell structure was synthesized by a solvothermal procedure.[33] In brief, for the synthesis of the core nanoparticles, anhydrous $Y(CH_3CO_2)_3$ (372 mg), $Yb(CH_3CO_2)_3$ (210 mg), and $Tm(CH_3CO_2)_3$ (3.5 mg) were added to a 100 mL two-neck round-bottom flask containing oleic acid (35 mL). The solution was first purged with N_2 and then heated slowly to 110 ºC under reduced pressure until complete removal of residual water and oxygen. The temperature of the reaction flask was then lowered to 50 ºC under a gentle N_2 flow. During this time, an anhydrous methanol solution of ammonium fluoride (0.3 g) and sodium hydroxide (0.4 g) was prepared via sonication, and the mixture solution was then transferred to the two-neck flask via cannulation. The reaction flask was heated to 65 ºC under reduced pressure until complete removal of methanol. Subsequently, the reaction temperature was increased to 300 ºC as quick as possible and maintained at this temperature for 30 min under N_2. After reaction, the nanoparticles were

precipitated by adding excess ethanol (400 mL) and collected by centrifugation at 4500 rpm. The resulting pellet was redispersed in hexane and precipitated with excess ethanol. The dispersion-precipitation process was repeated until the removal of free oleic acids. The core-shell UCNPs with an outer layer of $NaYF_4$ was synthesized following the same solvolthermal procedure except that the reaction time was increased to 90 min.

For the synthesis of citrate-modified UCNPs, 100 mg of core-shell UCNPs was dispersed in 60 mL of diethylene glycol (DEG) followed by adding 200 mg of trisodium citrate. The mixture was then heated to 200 ^oC with gentle stirring for 17 h. After cooling to room temperature, the modified UCNPs were collected by centrifugation under 12000 rpm. The precipitate was rinsed with 20 mL of DEG for 3 times to remove nonadsorbed citrate ligands followed by rinsed with 20 mL of CH_2Cl_2 to remove DEG. The final product was obtained by drying under room temperature.

For the synthesis of dendrimer-encapsulated UCNPs via LBL method, 20 mg of citrate-modified UCNPs was dispersed in 15 mL of H_2O followed by adding 40 μL of NH_2-terminated PAMAM dendrimer (10 wt% in methanol). The mixture solution was then carefully adjusted to pH = 4 by adding HCl solution and allowed to stirring at room temperature for 24 h. After reaction, water was first removed by vacuum distillation, and the modified UCNPs was precipitated by adding 200 mL of cold acetone. The final product collected by centrifugation under 12000 rpm was drying under vacuum under the temperature less than 35 ^oC.

For the synthesis of hybrid UCNPs, 10 mg of the dendrimer-encapsulated UCNPs was dispersed in 5 mL of methanol with gentle stirring followed by adding Ce6 stock solution (1.5×10^{-3} M in methanol). The feeding amount of Ce6 was fine adjusted by controlling the injection volume of the stock solution. The mixture solution was stirred under room temperature for 2 h, and the solvent was removed under reduced pressure. The crude UCNPs was rinsed with CH_2Cl_2 to wash off the nonadsorbed Ce6 until the CH_2Cl_2 layer was colorless. The final hybrid nanoparticles was drying under room temperature, and the loading capacity of the Ce6 was determined by fluorescence spectroscopy analysis. Prior to biological experiments, the hybrid UCNPs was prepared in stock aqueous solutions with corresponding Ce6 concentrations of 0.43, 2.50 and 13.6 μM.

2.3 The $^1O_2$ assay

In a typical FCLA experiment, 20 μL of a FCLA/ethanol solution (0.7 mg/mL) was added to 2 mL of a UCNPs solution and transferred into a 1-cm quartz cuvette. The solution was irradiated with an either 660- or 980-nm laser diode, and the emission intensity of the exposed solutions at 519-nm was recorded every 2 min under 496-nm excitation by fluorescence spectroscopy. For the control experiment, FCLA emission was also recorded at the same conditions in the absence of laser irradiation.

2.4 Cell culture and tumorsphere cultivation

For a conventional 2D cell model, MCF-7 cells was obtained from American Type Culture Collection (Manassas, VA, USA) and cultured in DMEM medium (Invitrogen Corporation, Grand Island, NY, USA) containing 10% fetal bovine serum (Invitrogen) and 5 μg/mL insulin (Sigma-Aldrich, St. Louis, MO, USA). For a 3D tumorsphere cultivation, MCF-7 cells were prepared as a density of 1×10^4 cells/mL in DMEM/F12 medium (Invitrogen Corporation) containing 0.5% methylcellulose (Sigma-Aldrich), 0.4% bovine serum albumin (Sigma-Aldrich), 10 ng/mL of EGF (PeproTech, Rocky Hill, NJ, USA), 10 ng/mL bFGF (PeproTech), 5 μg/mL insulin, 1 μM hydrocortisone (Sigma-Aldrich) and 4 μg/mL heparin (Sigma-Aldrich). Cell suspension (2 mL) was seeded into wells of suspension culture 6-well-plate (Greiner Bio One International GmbH, Frickenhausen Germany) and incubated for 7 days.

2.5 Cell viability assay

To determine the PDT efficiency, cell proliferation for the cells cultured in a 2D model after light

exposure were determined by CCK8 cell viability assay reagent (Sigma-Aldrich) using a microplate reader (Molecular Devices, Sunnyvale, CA, USA) according to the manufacturer's recommendations. For the in vitro photoexicitation experiment, MCF-7 cells were firstly suspended as 1×10^5/ml for 2.5 ml and transferred into a 1-cm quartz cuvette and directly exposed to a laser beam with either 660- or 980-nm wavelength at fixed time intervals under gentle agitation. The exposed cells were then seeded into 96-well-plate at 1×10^4/well and cultured for another 48 h. The absorbance values at 440 nm of non-treatment control were set as 100% of cell proliferation. Cell proliferation for the cells cultivated in a 3D model were determined by LIVE/DEAD cell viability assay (Thermo Fisher Scientific, Waltham, MA, USA). The viable or dead cells were specifically stained by green and red fluorophores derived from calcein AM and ethidium homodimer-1, respectively. Following the same protocol of the in vitro photoexcitation, the exposed tumorspheres were collected and washed by phosphate based saline followed by suspended in 250 μl PBS containing 4 μM of calcien AM/2 μM of ethidium homodimer-1. After incubation at 37°C for 30 minutes, fluorescence images with respect to the distributions of viable and dead cells in tumorspheres were captured by inverted fluorescence microscopy (AE30, Motic Electric Group Co., Ltd., Xiamen, China) and counted with ImageJ software (NIH, Bethesda. MA, USA).

Acknowledgments
The authors would like to thank Chung Shan Medical University and Ministry of Science and Technology (MOST) of Taiwan, for financially supporting this research (MOST104-2119-M-040-001) and for instrumental analysis. The authors are also grateful to Prof. Jing-Yun Wu from National Chi-Nan University for support with TGA analysis and to Prof. Hsien-Ming Lee from Academic Sinica for support with dynamic light scattering analysis.

Supplementary data
Supplementary data related to this article can be found at http://

References
1. G. Chen, H. Qiu, P. N. Prasad and X. Chen, *Chem. Rev.*, 2014, **114**, 5161-5214.
2. V. Shanmugam, S. Selvakumar and C.-S. Yeh, *Chem. Soc. Rev.*, 2014, **43**, 6254-6287.
3. J. Li, W. Y.-W. Lee, T. Wu, J. Xu, K. Zhang, D. S. Hong Wong, R. Li, G. Li and L. Bian, *Biomaterials*, 2016, **110**, 1-10.
4. C. Wang, X. Li and F. Zhang, *Analyst*, 2016, **141**, 3601-3620.
5. Y. Xu, J. Xiang, H. Zhao, H. Liang, J. Huang, Y. Li, J. Pan, H. Zhou, X. Zhang, J. H. Wang, Z. Liu and J. Wang, *Biomaterials*, 2016, **100**, 91-100.
6. G. Tian, X. Zheng, X. Zhang, W. Yin, J. Yu, D. Wang, Z. Zhang, X. Yang, Z. Gu and Y. Zhao, *Biomaterials*, 2015, **40**, 107-116.
7. A. Punjabi, X. Wu, A. Tokatli-Apollon, M. El-Rifai, H. Lee, Y. Zhang, C. Wang, Z. Liu, E. M. Chan, C. Duan and G. Han, *ACS Nano*, 2014, **8**, 10621-10630.
8. G. Tian, Z. Gu, L. Zhou, W. Yin, X. Liu, L. Yan, S. Jin, W. Ren, G. Xing, S. Li and Y. Zhao, *Adv. Mater.*, 2012, **24**, 1226-1231.
9. S. Yang, N. Li, Z. Liu, W. Sha, D. Chen, Q. Xu and J. Lu, *Nanoscale*, 2014, **6**, 14903-14910.
10. H. Qiu, C. Yang, W. Shao, J. Damasco, X. Wang, H. Ågren, P. Prasad and G. Chen, *Nanomaterials*, 2014, **4**, 55.
11. X. Wang, C.-X. Yang, J.-T. Chen and X.-P. Yan, *Anal. Chem.*, 2014, **86**, 3263-3267.
12. M. Wang, Z. Chen, W. Zheng, H. Zhu, S. Lu, E. Ma, D. Tu, S. Zhou, M. Huang and X. Chen, *Nanoscale*, 2014, **6**, 8274-8282.

13. C. Wang, L. Cheng, Y. Liu, X. Wang, X. Ma, Z. Deng, Y. Li and Z. Liu, *Adv. Funct. Mater.*, 2013, **23**, 3077-3086.
14. X. Liu, M. Zheng, X. Kong, Y. Zhang, Q. Zeng, Z. Sun, W. J. Buma and H. Zhang, *Chem. Commun.*, 2013, **49**, 3224-3226.
15. V. Rapozzi and G. Jori, *Resistance to Photodynamic Therapy in Cancer*, Springer International Publishing, Switzerland, 2015.
16. L. Zhao, J. Peng, Q. Huang, C. Li, M. Chen, Y. Sun, Q. Lin, L. Zhu and F. Li, *Adv. Funct. Mater.*, 2014, **24**, 363-371.
17. H. S. Qian, H. C. Guo, P. C.-L. Ho, R. Mahendran and Y. Zhang, *Small*, 2009, **5**, 2285-2290.
18. X.-J. Wu and D. Xu, *J. Am. Chem. Soc.*, 2009, **131**, 2774-2775.
19. S. J. Budijono, J. Shan, N. Yao, Y. Miura, T. Hoye, R. H. Austin, Y. Ju and R. K. Prud'homme, *Chem. Mater.*, 2010, **22**, 311-318.
20. N. Bogdan, F. Vetrone, R. Roy and J. A. Capobianco, *J. Mater. Chem.*, 2010, **20**, 7543-7550.
21. E. Mohammadifar, A. Nemati Kharat and M. Adeli, *J. Mater. Chem. B*, 2015, **3**, 3896-3921.
22. H. Liu, M. Shen, J. Zhao, J. Zhu, T. Xiao, X. Cao, G. Zhang and X. Shi, *Analyst*, 2013, **138**, 1979-1987.
23. I. Matai and P. Gopinath, *ACS Biomater. Sci. Eng.*, 2016, **2**, 213-223.
24. A. Siriviriyanun, T. Imae, G. Calderó and C. Solans, *Colloids Surf. B. Biointerfaces*, 2014, **121**, 469-473.
25. E. R. Figueroa, A. Y. Lin, J. Yan, L. Luo, A. E. Foster and R. A. Drezek, *Biomaterials*, 2014, **35**, 1725-1734.
26. D. A. Tomalia, H. Baker, J. Dewald, M. Hall, G. Kallos, S. Martin, J. Roeck, J. Ryder and P. Smith, *Polym. J.*, 1985, **17**, 117-132.
27. J. G. Worden, Q. Dai and Q. Huo, *Chem. Commun.*, 2006, 1536-1538.
28. Y.-J. Tsai, C.-C. Hu, C.-C. Chu and T. Imae, *Biomacromolecules*, 2011, **12**, 4283-4290.
29. L.-B. Weiswald, D. Bellet and V. Dangles-Marie, *Neoplasia*, 2015, **17**, 1-15.
30. M. Alemany-Ribes, M. García-Díaz, M. Busom, S. Nonell and C. E. Semino, *Tissue Eng., Part A*, 2013, **19**, 1665-1674.
31. X. Huang, X.-J. Tian, W.-l. Yang, B. Ehrenberg and J.-Y. Chen, *PCCP*, 2013, **15**, 15727-15733.
32. H. Gong, Z. Dong, Y. Liu, S. Yin, L. Cheng, W. Xi, J. Xiang, K. Liu, Y. Li and Z. Liu, *Adv. Funct. Mater.*, 2014, **24**, 6492-6502.
33. J.-C. Boyer, C.-J. Carling, B. D. Gates and N. R. Branda, *J. Am. Chem. Soc.*, 2010, **132**, 15766-15772.
34. F. Vetrone, R. Naccache, V. Mahalingam, C. G. Morgan and J. A. Capobianco, *Adv. Funct. Mater.*, 2009, **19**, 2924-2929.
35. H.-P. Zhou, C.-H. Xu, W. Sun and C.-H. Yan, *Adv. Funct. Mater.*, 2009, **19**, 3892-3900.
36. D. Wang, C. Chen, X. Ke, N. Kang, Y. Shen, Y. Liu, X. Zhou, H. Wang, C. Chen and L. Ren, *ACS Appl. Mater. Interfaces*, 2015, **7**, 3030-3040.
37. L. Tong, E. Lu, J. Pichaandi, P. Cao, M. Nitz and M. A. Winnik, *Chem. Mater.*, 2015, **27**,

4899-4910.
38. C.-C. Chu and T. Imae, *Macromol. Rapid Commun.*, 2009, **30**, 89-93.
39. W. I. Lee, Y. Bae and A. J. Bard, *J. Am. Chem. Soc.*, 2004, **126**, 8358-8359.
40. D. Wang and T. Imae, *J. Am. Chem. Soc.*, 2004, **126**, 13204-13205.
41. X. Chen, Z. Zhao, M. Jiang, D. Que, S. Shi and N. Zheng, *New J. Chem.*, 2013, **37**, 1782-1788.
42. C. Wang, H. Tao, L. Cheng and Z. Liu, *Biomaterials*, 2011, **32**, 6145-6154.
43. Q. Q. Dou, C. P. Teng, E. Ye and X. J. Loh, *Int. J. Nanomed.*, 2015, **10**, 419-432.
44. C.-H. Lee, C.-C. Yu, B.-Y. Wang and W.-W. Chang, *Oncotarget*, 2015, **7**, 1215-1226.
45. C.-Y. Peng, P.-C. Fong, C.-C. Yu, W.-C. Tsai, Y.-M. Tzeng and W.-W. Chang, *Molecules*, 2013, **18**, 2539.
46. Y.-C. Chen, X. Lou, Z. Zhang, P. Ingram and E. Yoon, *Sci. Rep.*, 2015, **5**, 12175.

科技部補助計畫衍生研發成果推廣資料表

日期:2017/03/01

科技部補助計畫	計畫名稱: 具有可見光與近紅外光吸收能力的光敏感兩親性樹枝狀分子載體:材料合成與光誘導控制釋放性質分析
	計畫主持人: 朱智謙
	計畫編號: 104-2119-M-040-001- 學門領域: 有機化學

無研發成果推廣資料

104年度專題研究計畫成果彙整表

計畫主持人：朱智謙	**計畫編號：**104-2119-M-040-001-
計畫名稱：具有可見光與近紅外光吸收能力的光敏感兩親性樹枝狀分子載體:材料合成與光誘導控制釋放性質分析	

成果項目					量化	單位	質化 （說明：各成果項目請附佐證資料或細項說明，如期刊名稱、年份、卷期、起訖頁數、證號...等）
國內	學術性論文	期刊論文			0	篇	
		研討會論文			2		
		專書			0	本	
		專書論文			0	章	
		技術報告			0	篇	
		其他			0	篇	
	智慧財產權及成果	專利權	發明專利	申請中	1	件	
				已獲得	0		
			新型/設計專利		0		
		商標權			0		
		營業秘密			0		
		積體電路電路布局權			0		
		著作權			0		
		品種權			0		
		其他			0		
	技術移轉	件數			0	件	
		收入			0	千元	
國外	學術性論文	期刊論文			2	篇	
		研討會論文			0		
		專書			0	本	
		專書論文			0	章	
		技術報告			0	篇	
		其他			0	篇	
	智慧財產權及成果	專利權	發明專利	申請中	0	件	
				已獲得	0		
			新型/設計專利		0		
		商標權			0		
		營業秘密			0		
		積體電路電路布局權			0		
		著作權			0		
		品種權			0		

		其他	0		
	技術移轉	件數	0	件	
		收入	0	千元	
參與計畫人力	本國籍	大專生	3	人次	
		碩士生	2		
		博士生	0		
		博士後研究員	0		
		專任助理	1		
	非本國籍	大專生	0		
		碩士生	0		
		博士生	0		
		博士後研究員	0		
		專任助理	0		
其他成果 （無法以量化表達之成果如辦理學術活動、獲得獎項、重要國際合作、研究成果國際影響力及其他協助產業技術發展之具體效益事項等，請以文字敘述填列。）					

科技部補助專題研究計畫成果自評表

請就研究內容與原計畫相符程度、達成預期目標情況、研究成果之學術或應用價值（簡要敘述成果所代表之意義、價值、影響或進一步發展之可能性）、是否適合在學術期刊發表或申請專利、主要發現（簡要敘述成果是否具有政策應用參考價值及具影響公共利益之重大發現）或其他有關價值等，作一綜合評估。

1. 請就研究內容與原計畫相符程度、達成預期目標情況作一綜合評估
   ■達成目標
   □未達成目標（請說明，以100字為限）
   　□實驗失敗
   　□因故實驗中斷
   　□其他原因
   說明：

2. 研究成果在學術期刊發表或申請專利等情形（請於其他欄註明專利及技轉之證號、合約、申請及洽談等詳細資訊）
   論文：□已發表　□未發表之文稿　■撰寫中　□無
   專利：□已獲得　■申請中　□無
   技轉：□已技轉　□洽談中　■無
   其他：（以200字為限）

3. 請依學術成就、技術創新、社會影響等方面，評估研究成果之學術或應用價值（簡要敘述成果所代表之意義、價值、影響或進一步發展之可能性，以500字為限）
   本計劃目標為光敏感型兩親性樹枝狀分子的合成製備、自組裝複合體的型態分析與物理化學性質分析、以及初步光控釋放效率的探討。自評目前的研究成果符合原先設定之目標。我們利用高效率的合成方法合成出一系列兩性基因載體，
   經過初步測試後證明此材料具有不錯的光控釋放能力。我們也嘗試利用Langmuir介面單分子層分析法來研究分子自組裝行為與光敏感現象。目前正在積極嘗試in vivo 細胞生物相關研究。另外，我們也開發出可利用近紅外光來驅動光動力療法的奈米複合材料，並成功的發現對於三維癌求幹細胞的深層治療效果。基於以上這些發現，除了能夠發表相關的學術論文之外，也可以思考與臨床醫學治療結合的可能性。

4. 主要發現
   本研究具有政策應用參考價值：■否　□是，建議提供機關
   （勾選「是」者，請列舉建議可提供施政參考之業務主管機關）
   本研究具影響公共利益之重大發現：■否　□是
   說明：（以150字為限）